Supplementary Information

Generic Synthesis of High Entropy Phosphides for Fast and Stable Li-Ion Storage

Wenwu Li[a], Yanhong Li[a],*, Jeng-Han Wang[b], Shengchi Huang[b], Anjie Chen[b], Lufeng Yang[e,f], Jie Chen[e,f], Lunhua He[f,g], Wei Kong Pang[h], Lar Thomsen[i], Bruce Cowie[i], Peixun Xiong[a], Yucun Zhou[d], Gun Jang[a], Dong Hyun Min[a], Jin Suk Byun[a], Lei Xu[j,k], Jia-Qi Huang[j,k], Kwang Chul Roh[l], Seo Hui Kang[l,m], Meilin Liu[d], Xiangfeng Duan[c],*, and Ho Seok Park[a,n,o,p],*

[a.] School of Chemical Engineering, Sungkyunkwan University, 2066, Seoburo, Jangan-gu, Suwon 440-746, Republic of Korea

[b.] Department of Chemistry, National Taiwan Normal University, Taipei, 11677, Taiwan

[c.] Department of Chemistry and Biochemistry, University of California, Los Angeles, CA 90095, USA

[d.] School of Materials Science & Engineering, Georgia Institute of Technology, Atlanta, GA 30332, USA

[e.] Institute of High Energy Physics, Chinese Academy of Sciences, Beijing, China.

[f.] Spallation Neutron Source Science Center, Dongguan, China.

[g.] Beijing National Laboratory for Condensed Matter Physics, Institute of Physics, Chinese Academy of Sciences, Beijing, China

[h.] Institute for Superconducting & Electronic Materials, University of Wollongong, Wollongong, NSW, Australia

[i.] Australian Synchrotron, Australian Nuclear Science and Technology Organization, Clayton Victoria 3168, Australia

[j.] School of Materials Science and Engineering, Beijing Institute of Technology, Beijing 100081, China

[k.] Advanced Research Institute of Multidisciplinary Science, Beijing Institute of Technology, Beijing 100081, China

[l.] Energy Storage Materials Center, Korea Institute of Ceramic Engineering and Technology, Jinju-Si, Gyeongsangnam-do 52851, Republic of Korea

[m.] Department of Materials Science and Engineering, Korea University, Anam-Dong, Seongbuk-Gu, Seoul 136-713, Republic of Korea

[n.] Department of Health Sciences and Technology, Samsung Advanced Institute for Health Sciences and Technology (SAIHST), Sungkyunkwan University, 2066, Seoburo, Jangan-gu, Suwon, 440-746, Republic of Korea

[o.] SKKU Advanced Institute of Nano Technology (SAINT), Sungkyunkwan University, 2066, Seoburo, Jangan-gu, Suwon, 440-746, Republic of Korea

[p.] SKKU Institute of Energy Science and Technology (SIEST), Sungkyunkwan University, 2066, Seoburo, Jangan-gu, Suwon 440-746, Republic of Korea

*Corresponding authors: yh.li9@siat.ac.cn (Y. Li), xduan@chem.ucla.edu (X. Duan), phs0727@skku.edu (H. S. Park),

1. Supplemental Methods:

**Electrochemical Measurements**

The calculation method of the lithium diffusion coefficient:

The data were collected by using galvanostatic intermittent titration technique (GITT)[1,2], charging and discharging for 10 min at a current density of 0.2 mA cm^{-2} followed by a 1.0 h rest. The lithium diffusion coefficient can be calculated for the following formula:

$$D_{Li^+} = \frac{4}{\pi}\left(\frac{iV_m}{Z_A FS}\right)^2 \left(\frac{(\frac{dE}{d\delta})}{(\frac{dE}{d\sqrt{t}})}\right)^2 \quad \frac{L^2}{D_{Li}} \quad (t << \overline{D_{Li}}) \quad (1)$$

where D_{Li^+} is the lithium-ion diffusion coefficient (cm^2 s^{-1}); i is the current density during the test process; V_m is the molar volume of the electrode (cm^2 mol^{-1}); Z_A is the charge number ("1" for Li-ion); F and S are the faraday constant (96485 C mol^{-1}) and the electrode/electrolyte contact area (cm^2), respectively; $\frac{dE}{d\delta}$ stands for the steady-state voltage change through the current pulse, $\frac{dE}{d\sqrt{t}}$ is the voltage change with a current pulse after deducing IR drop.
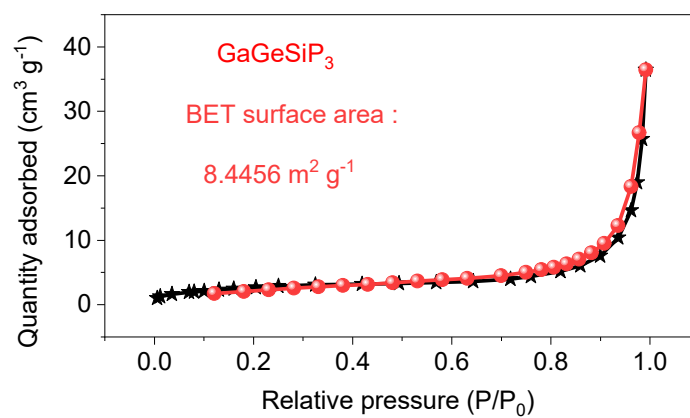
2. Supplemental Figures and Tables:
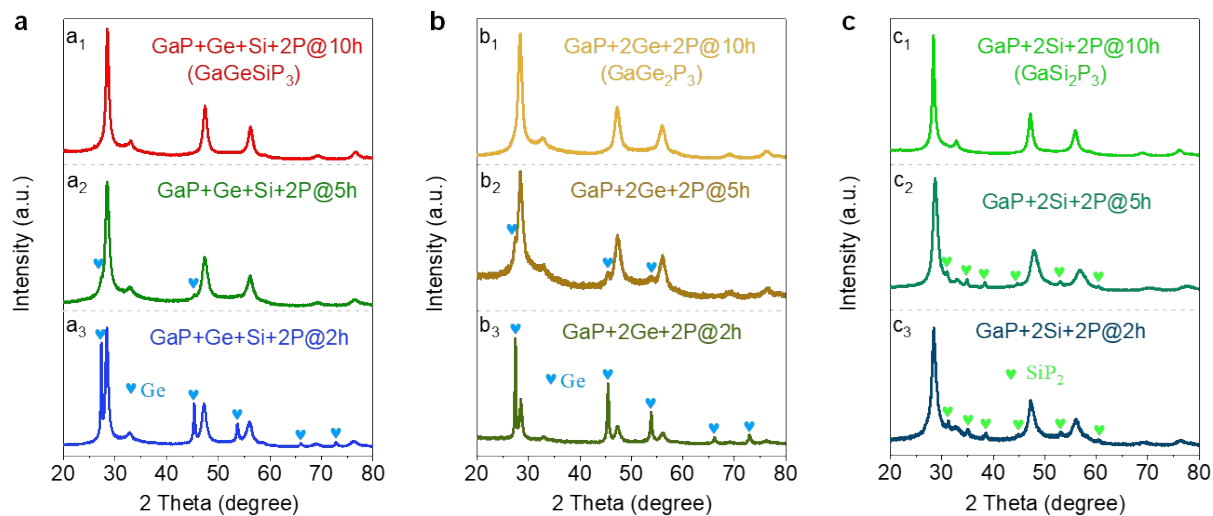
Fig. S1. Evolved XRD patterns.

(a) GaP+Ge+Si+2P@xh, (b) GaP+2Ge+2P@xh, and (c) GaP+2Si+2P@xh samples, where the x refers to the milling time.
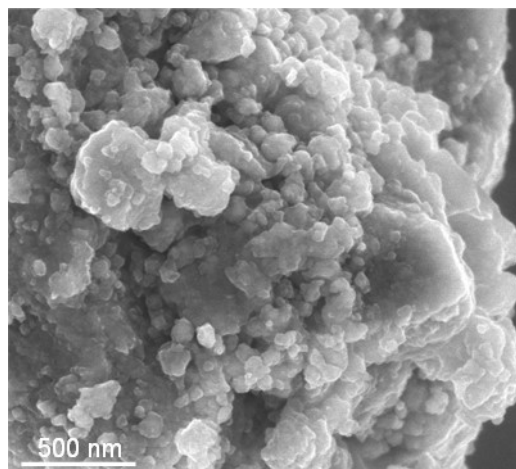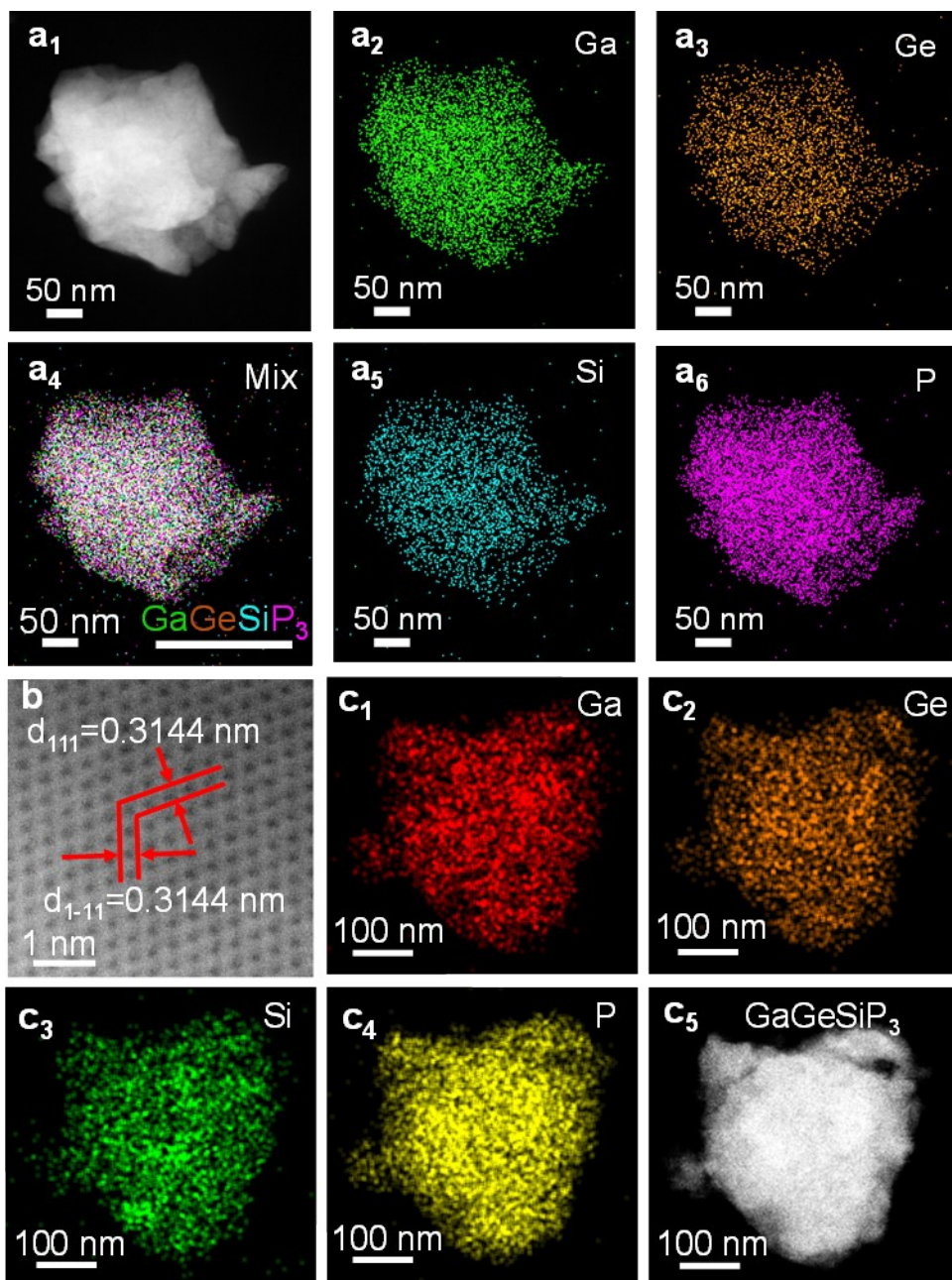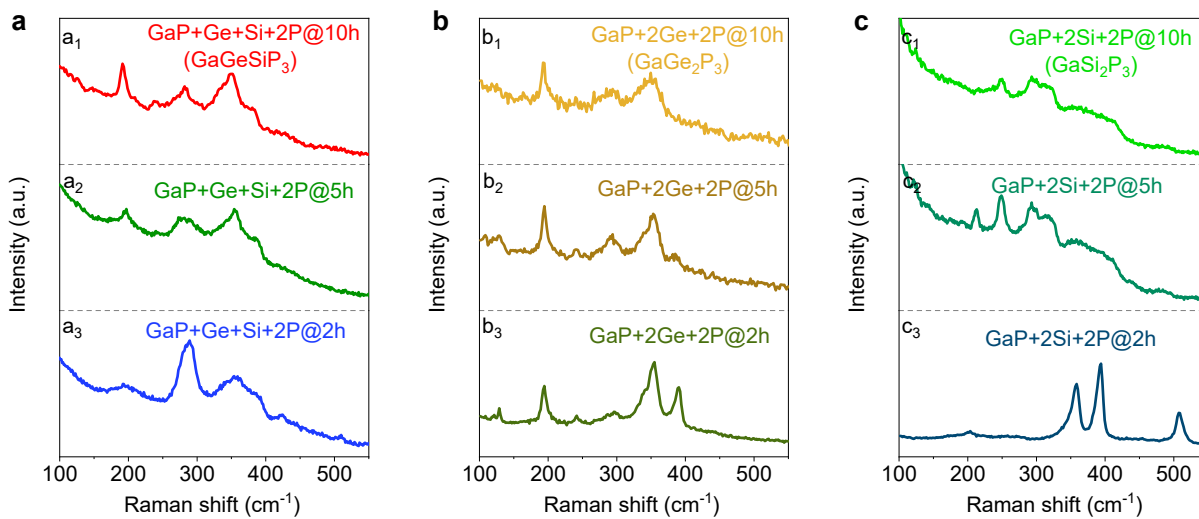
Fig. S2. Scanning electron microscopy image of GaGeSiP$_3$.

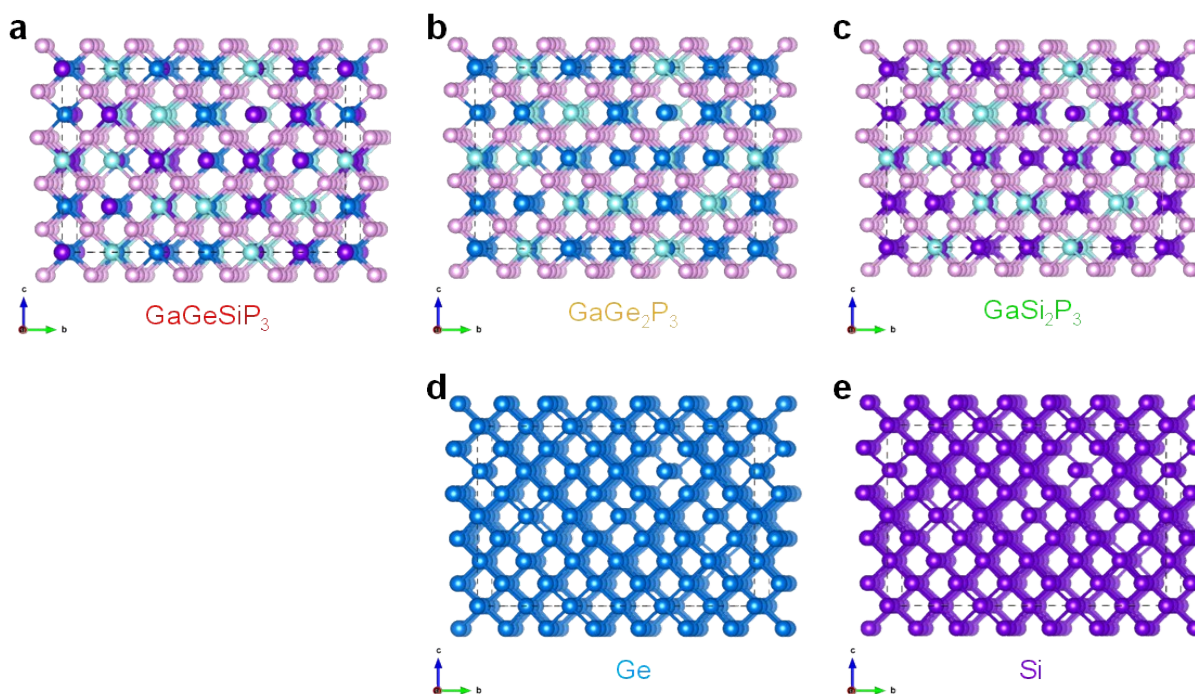**Fig. S3.** Brunner-Emmet-Teller (BET) profile of GaGeSiP$_3$.

Fig. S4. (a) Elemental mappings of GaGeSiP$_3$. (b) High resolution transmission electron microscope (HRTEM) image. (c) Elemental mappings of GaGeSiP$_3$.
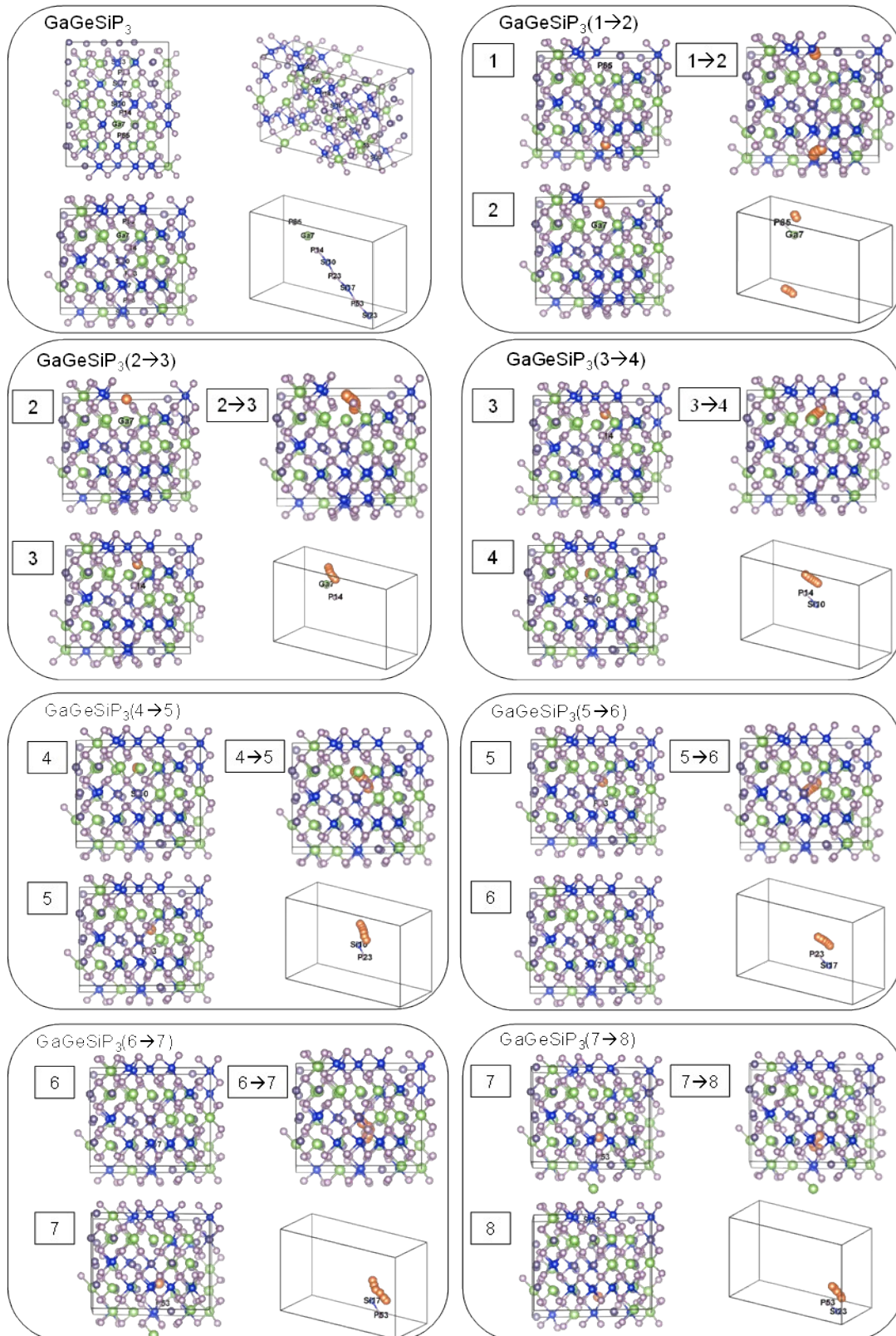
Fig. S5. Evolved Raman spectra.

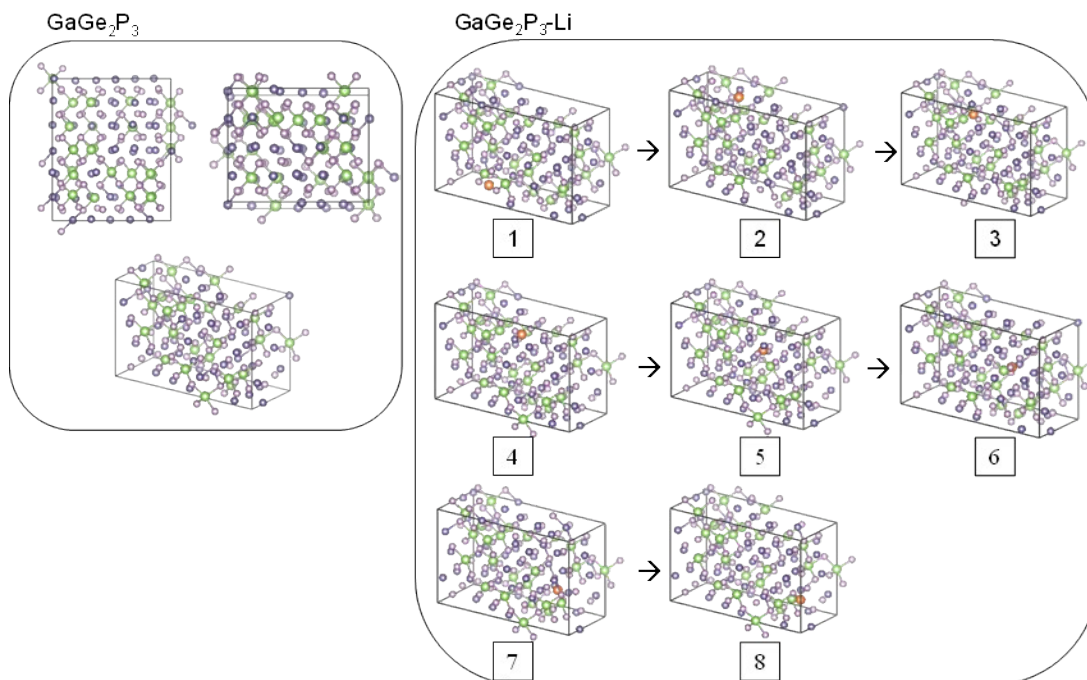(a) GaP+Ge+Si+2P@xh, (b) GaP+2Ge+2P@xh, and (c) GaP+2Si+2P@xh samples.

Fig. S6. 144-atom supercell models based on the special quasi-random structure (SQS) method.

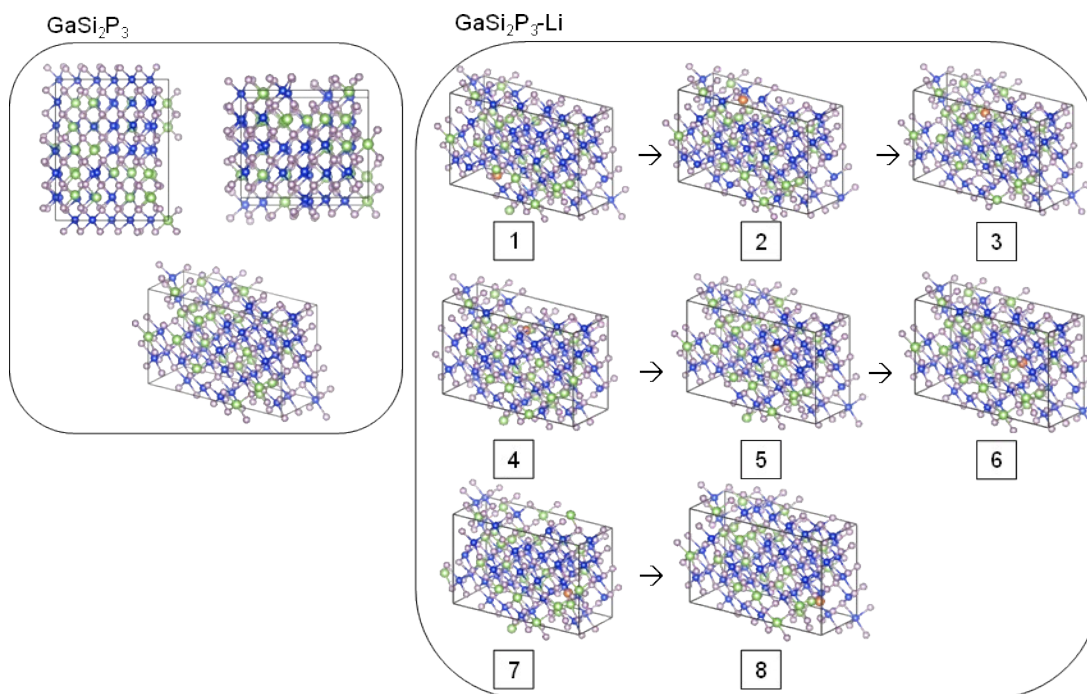(a) $GaGeSiP_3$, (b) $GaGe_2P_3$, (c) $GaSi_2P_3$, (d) Ge, and (e) Si.

Fig. S7. Li-ionic diffusion paths of the GaGeSiP$_3$. Li-ion diffusion energy barriers are shown in **Fig. 2a**.
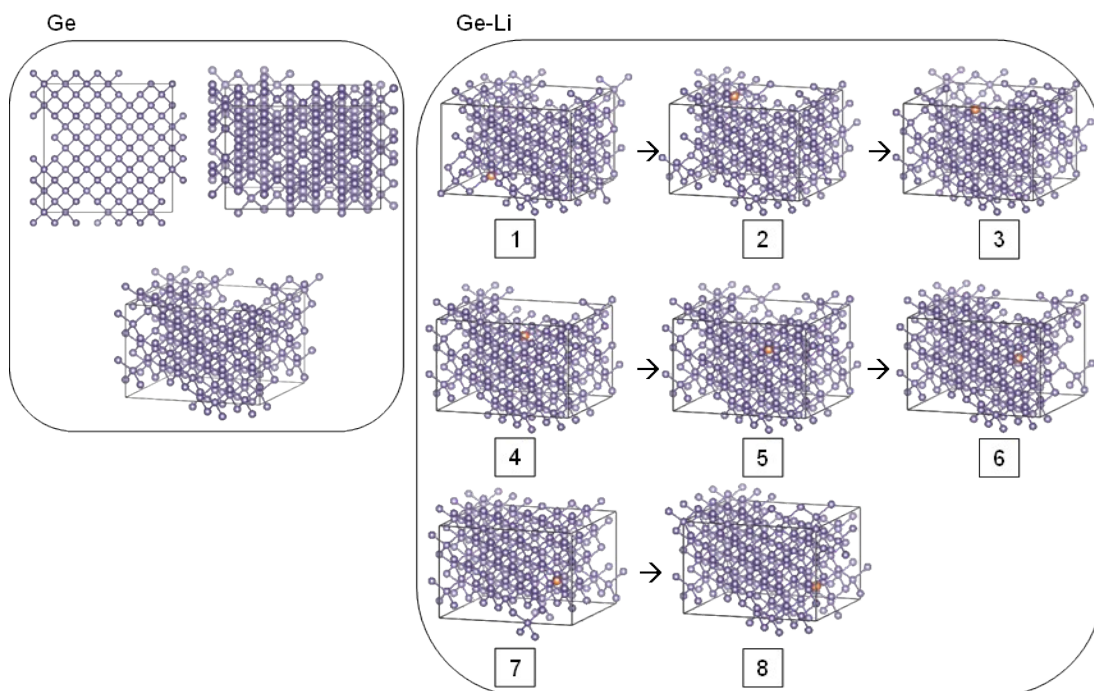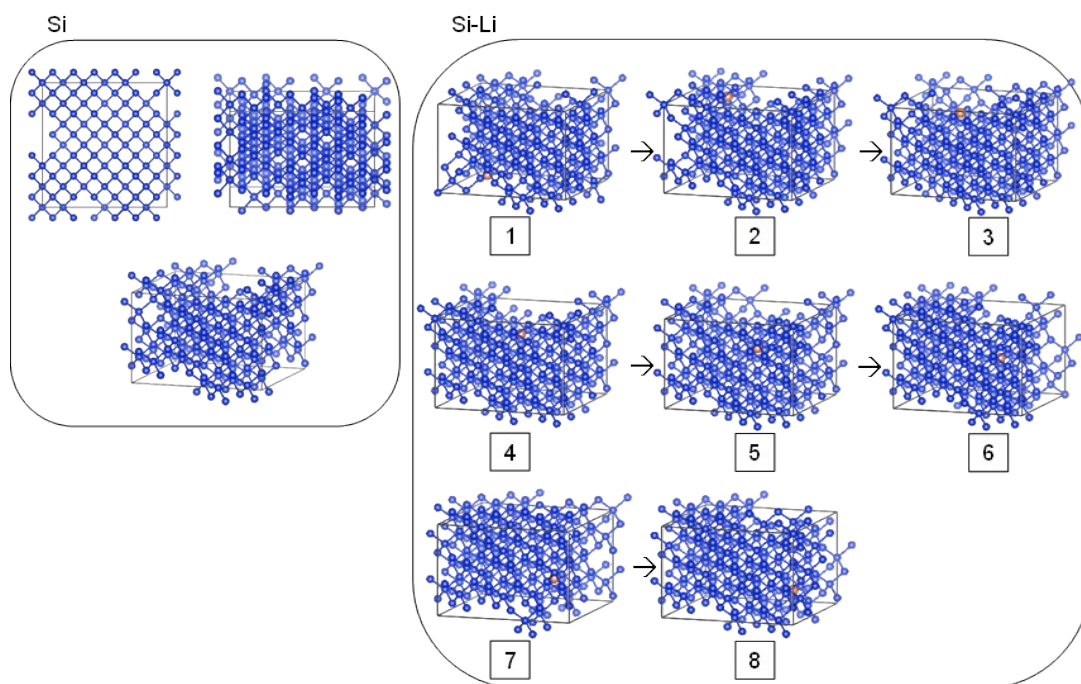
Fig. S8. Li-ionic diffusion paths of the $GaGe_2P_3$. Li-ionic transport energy barriers are marked in **Fig. 2a**.
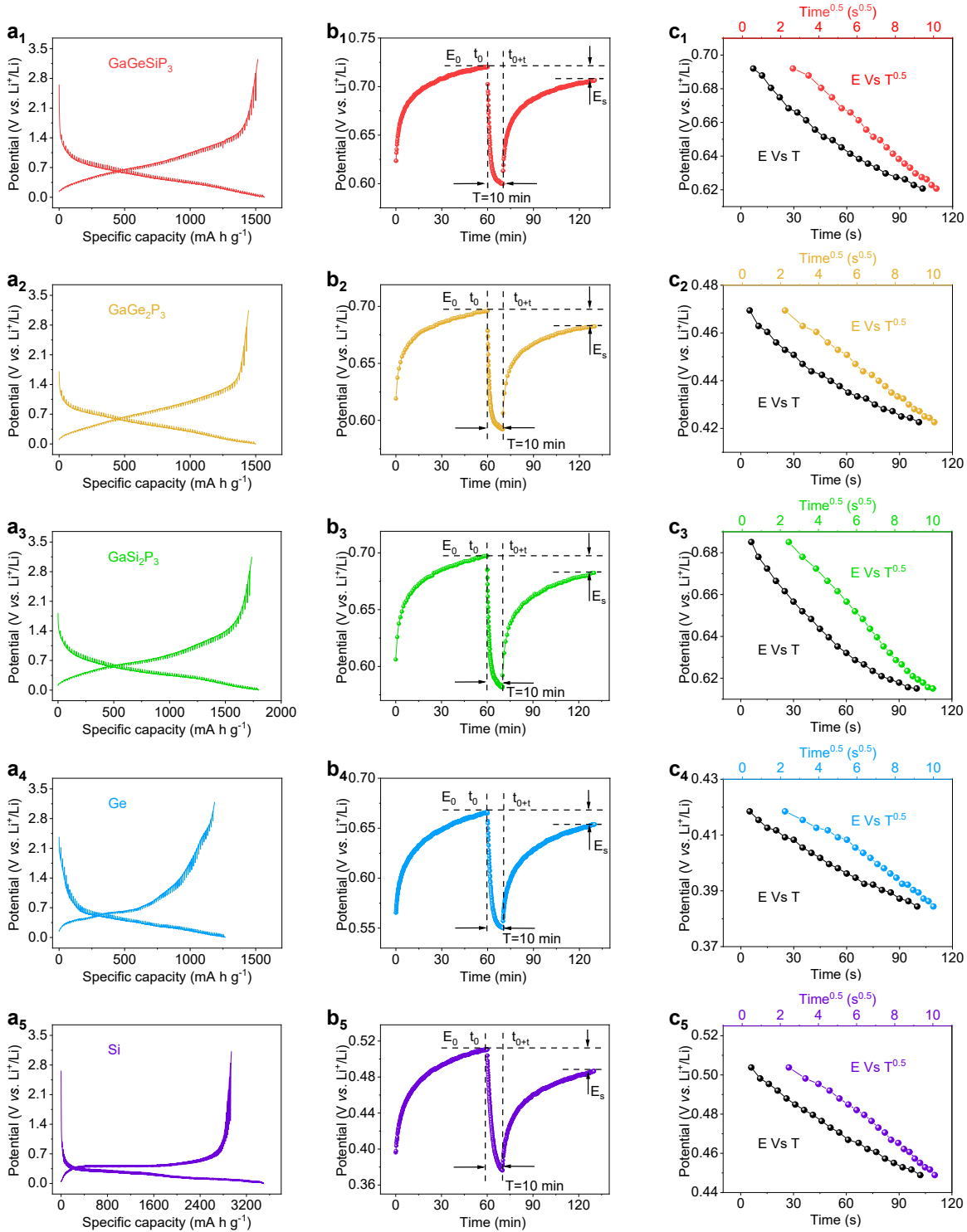

Fig. S9. Li-ionic diffusion paths of the $GaSi_2P_3$. Li-ion diffusion energy barriers are presented in **Fig. 2a**.

Fig. S10. Li-ionic diffusion paths of Ge. Li-ionic diffusion energy barriers are provided in **Fig. 2a**.


Fig. S11. Li-ionic diffusion paths of Si. Li-ion diffusion energy barriers are displayed in **Fig. 2a**.

Fig. S12. Galvanostatic intermittent titration technique (GITT) of GaGeSiP$_3$, GaGe$_2$P$_3$, GaSi$_2$P$_3$, Ge, and Si during the second GCD process.

(a) Potential vs. specific capacity profiles obtained through imposing a pulse time of 10 min and followed by a relaxation time of 1 h. (b) Potential vs. time during a single step of GITT test. (c) Linear fits of dE/dt$^{(1/2)}$ profiles in the first 100 s.
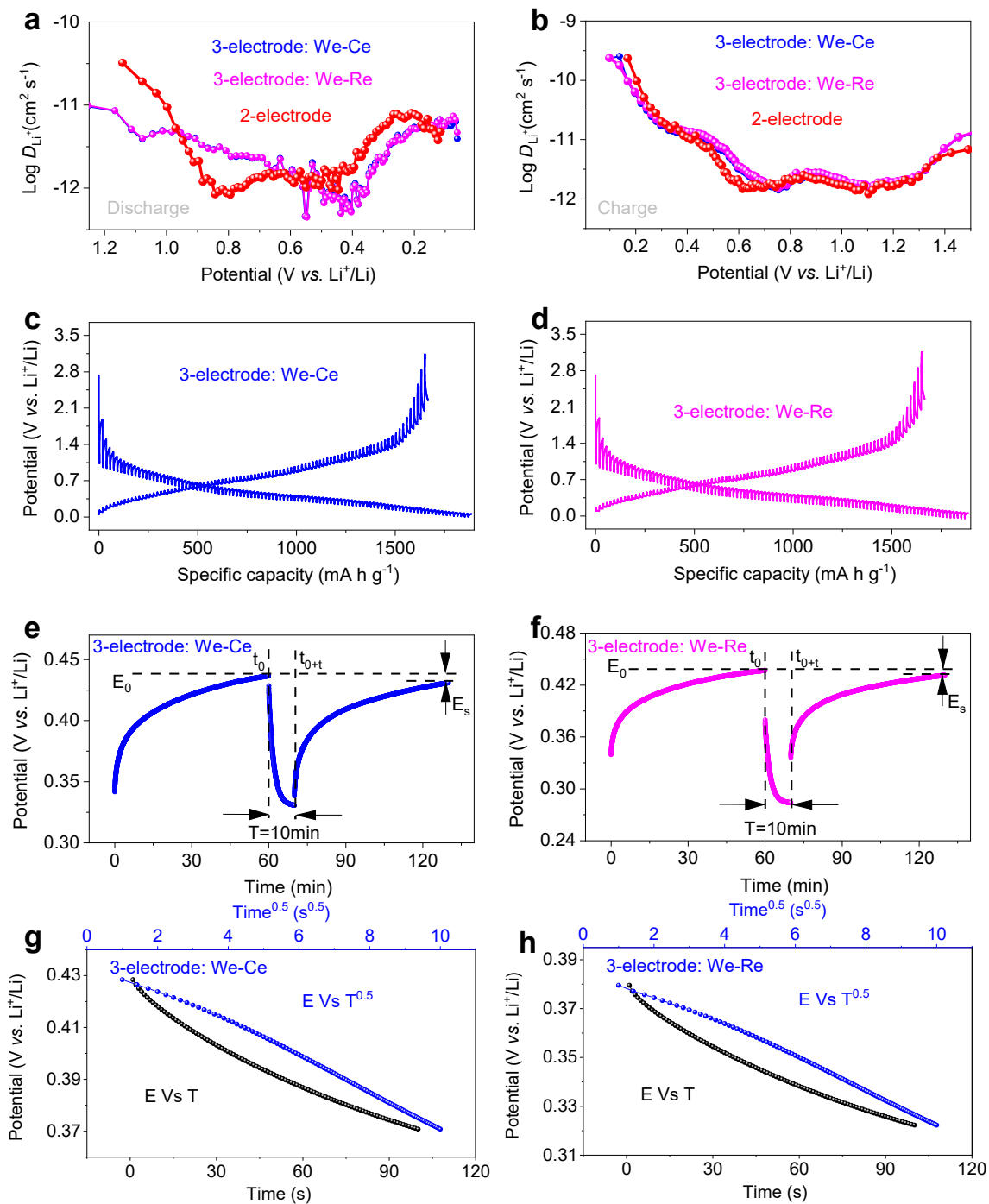
Fig. S13. Typical three-electrode configuration measurement data during the first cycle.
(a) Discharge process. (b) Charge process. (c-d) GCD profiles. (e) and (f) Potential vs. time during a single step of GITT test. (g) and (h) Linear fits of $dE/dt^{(1/2)}$ profiles in the first 100 s.

The Li-ionic diffusion coefficients from the three-electrode configuration measurements of the GaGeSiP$_3$ compound are comparable to the two-electrode configuration counterparts.
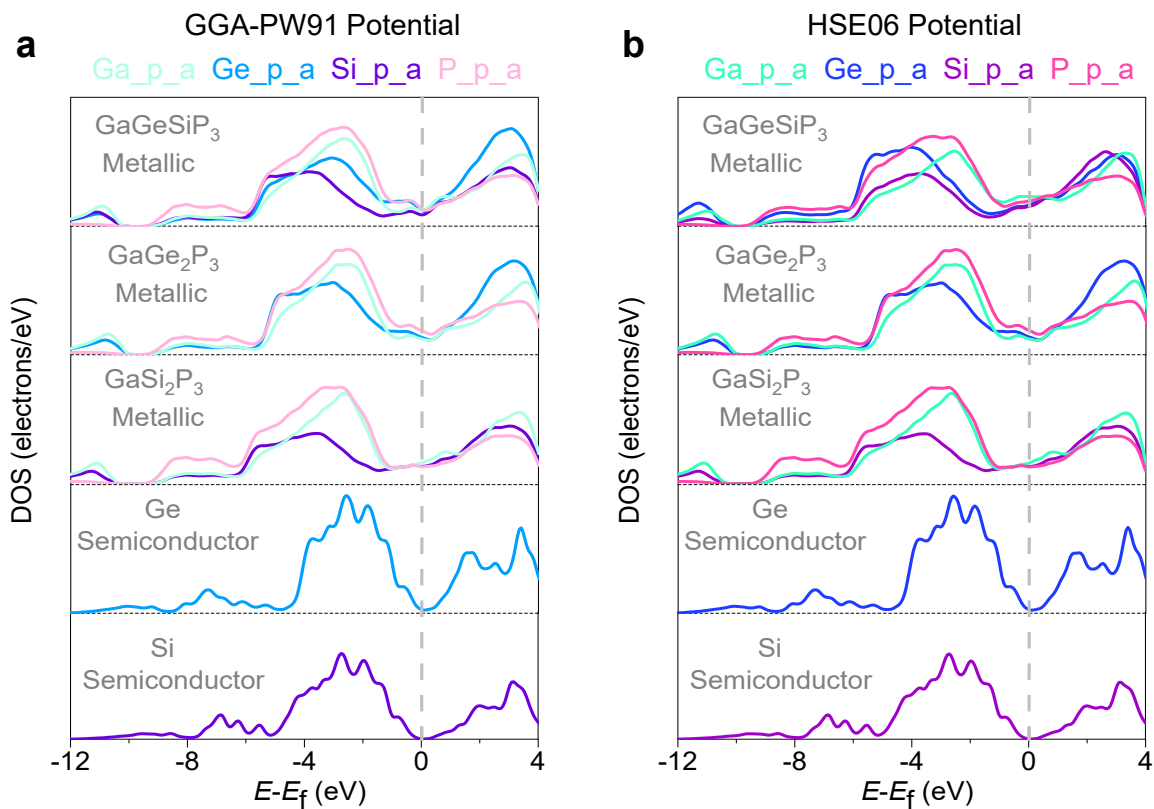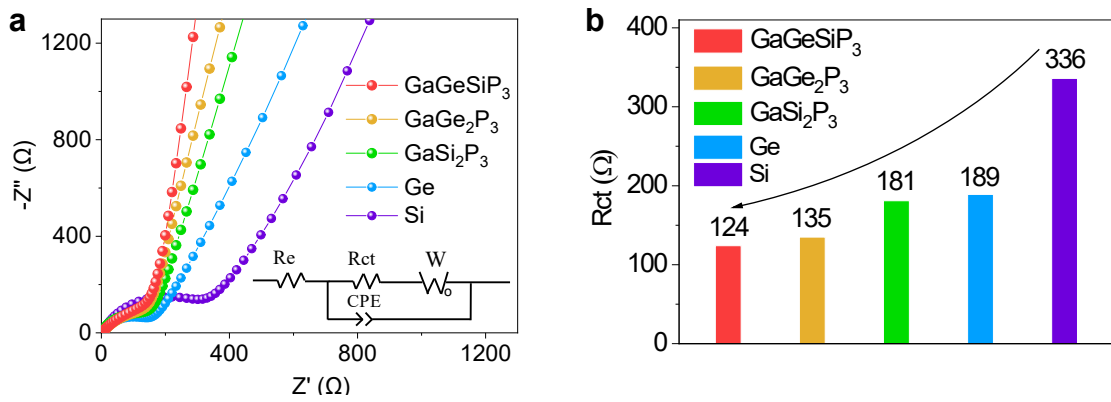
Fig. S14. Partial density of state (PDOS) profiles of GaGeSiP$_3$, GaGe$_2$P$_3$, GaSi$_2$P$_3$, Ge, and Si based on different potentials.

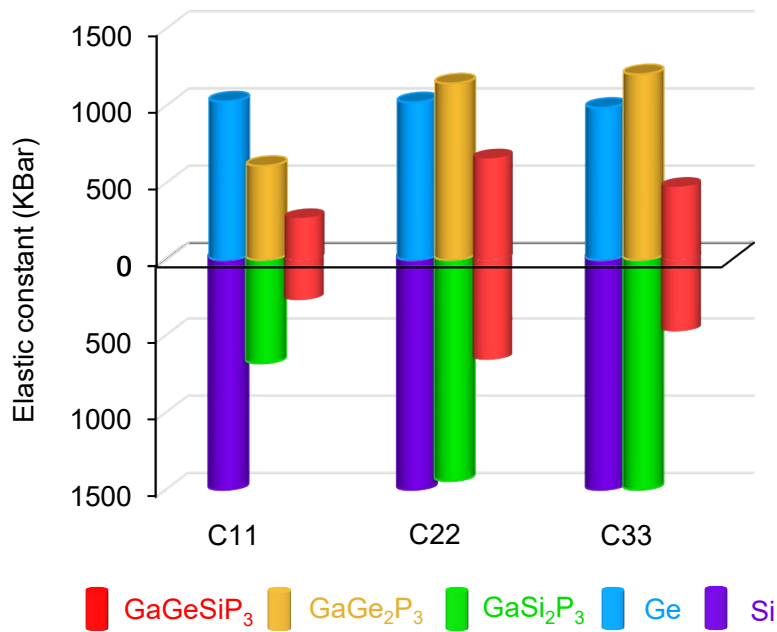(a) GGA-PW91 potential. (b) HSE potential.
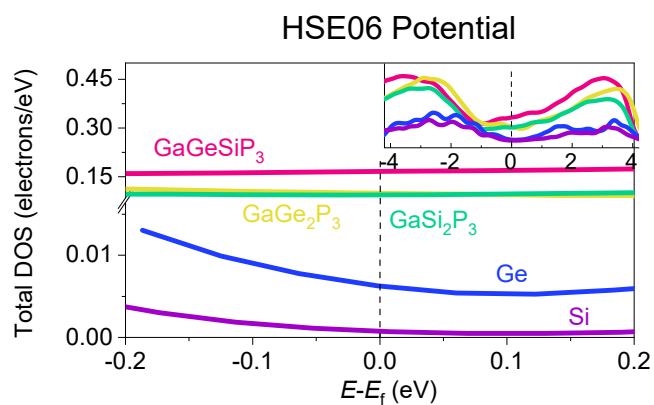
Fig. S15. Total density of state (TDOS) profiles of GaGeSiP$_3$, GaGe$_2$P$_3$, GaSi$_2$P$_3$, Ge, and Si based on HSE potential.
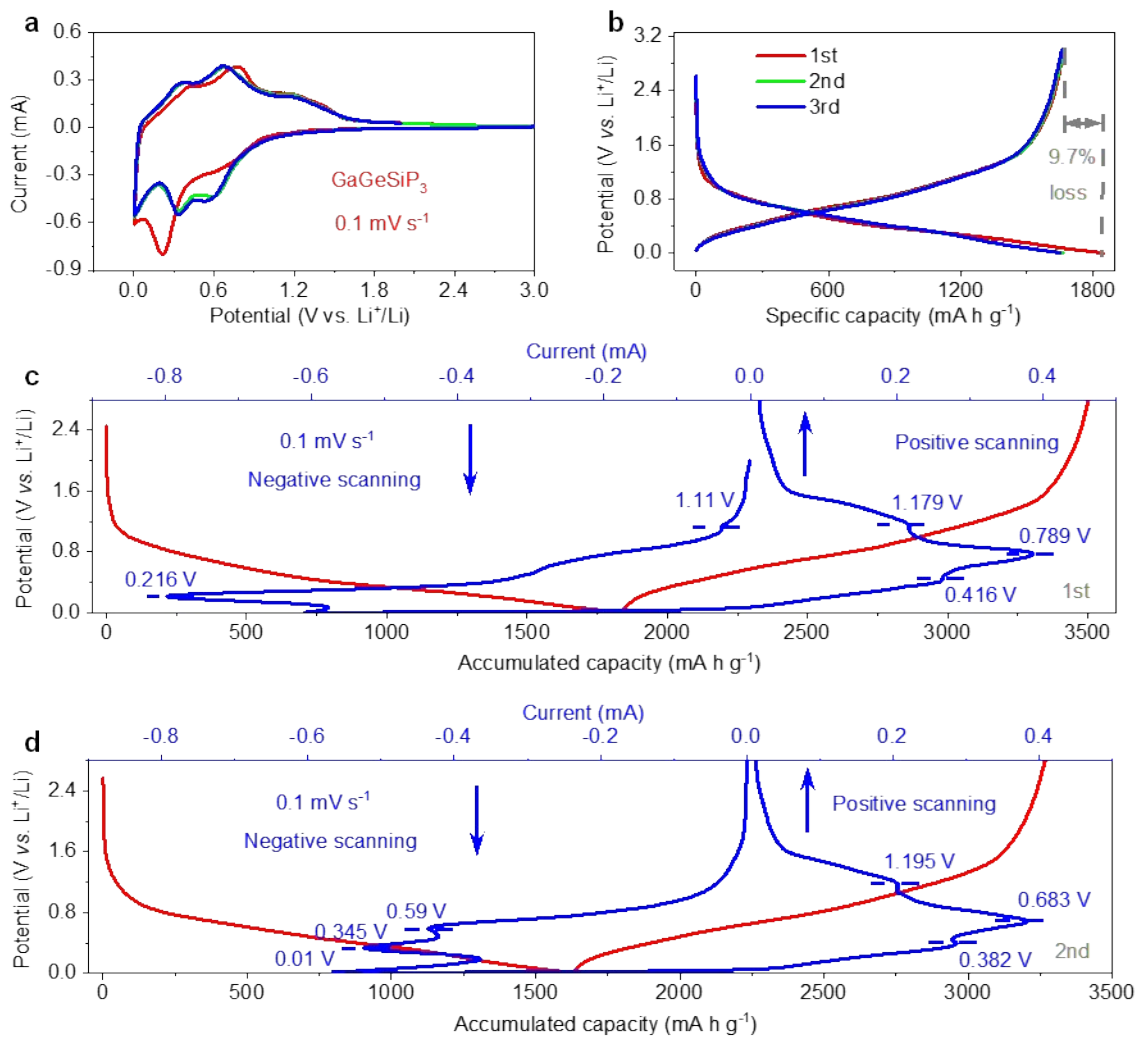
Fig. S16. (a) Electrochemical impedance spectra (EIS) and (b) Charge transfer resistance (R_{ct}) of GaGeSiP$_3$, GaGe$_2$P$_3$, GaSi$_2$P$_3$, Ge, and Si.
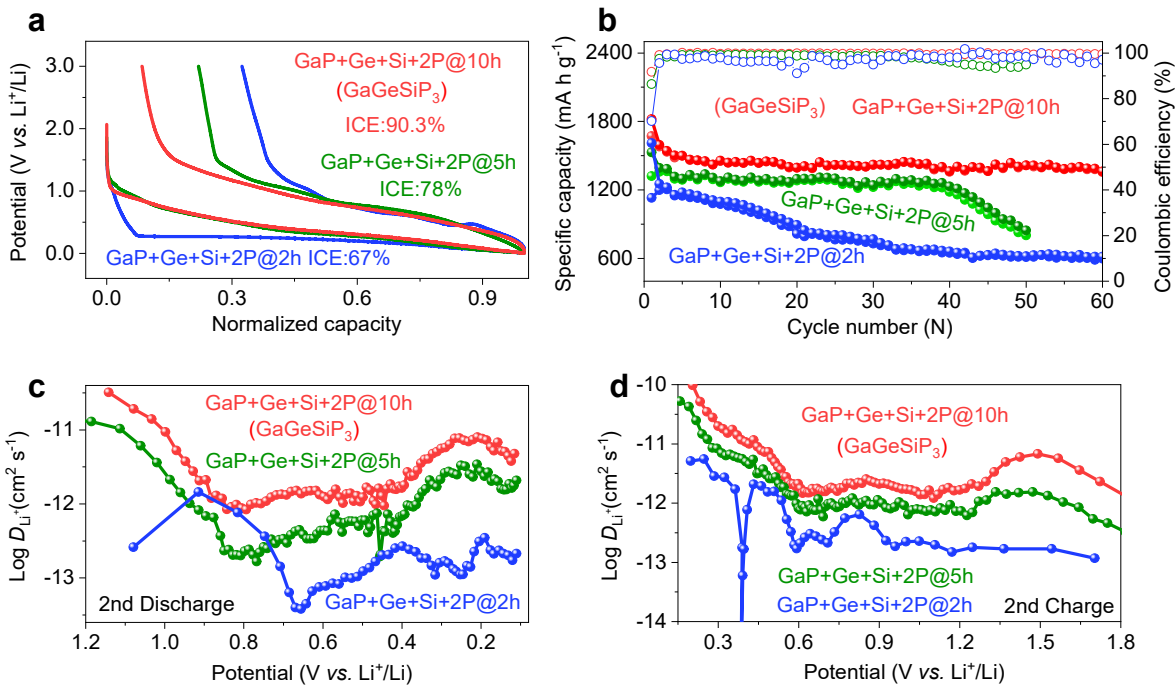

**Fig. S17.** Elastic constants of GaGeSiP$_3$, GaGe$_2$P$_3$, GaSi$_2$P$_3$, Ge, and Si.

Fig. S18. Electrochemical behaviors of GaGeSiP₃

(a) Initial three cyclic voltammetry (CV) profiles at 0.1 mV s⁻¹. (b) Initial three GCD profiles at 0.2 mA cm⁻². (c) First cycle. (D) Second cycle.
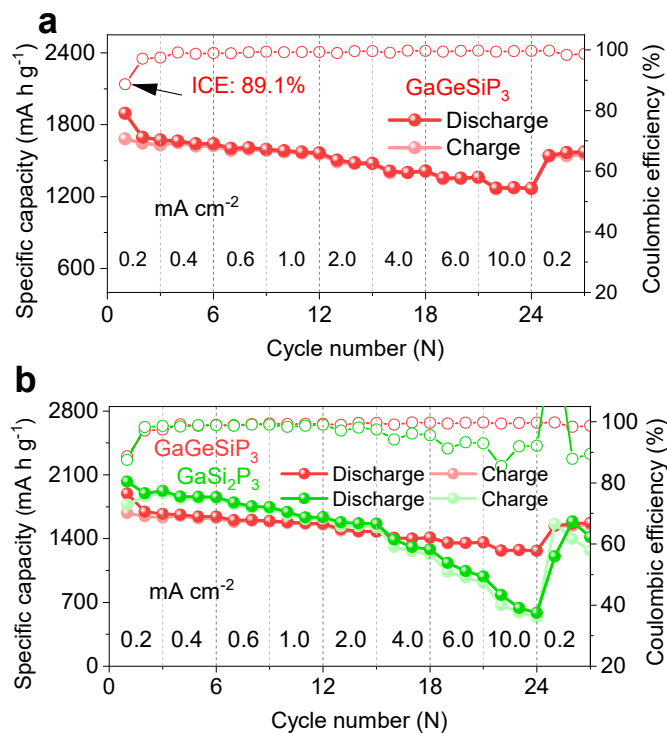
Fig. S19. Electrochemical behaviors of GaP+Ge+Si+2P@xh samples
(a) Initial GCD profiles at 0.2 mA cm^{-2}. (b) Cycle performances at 0.4 mA cm^{-2}. (c) and (d) Li-ionic diffusion coefficients at 0.2 mA cm^{-2}.
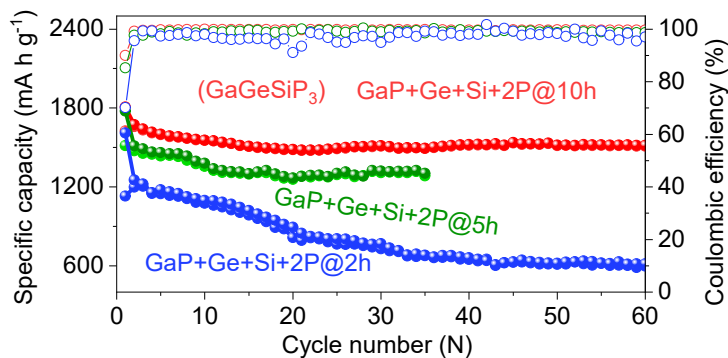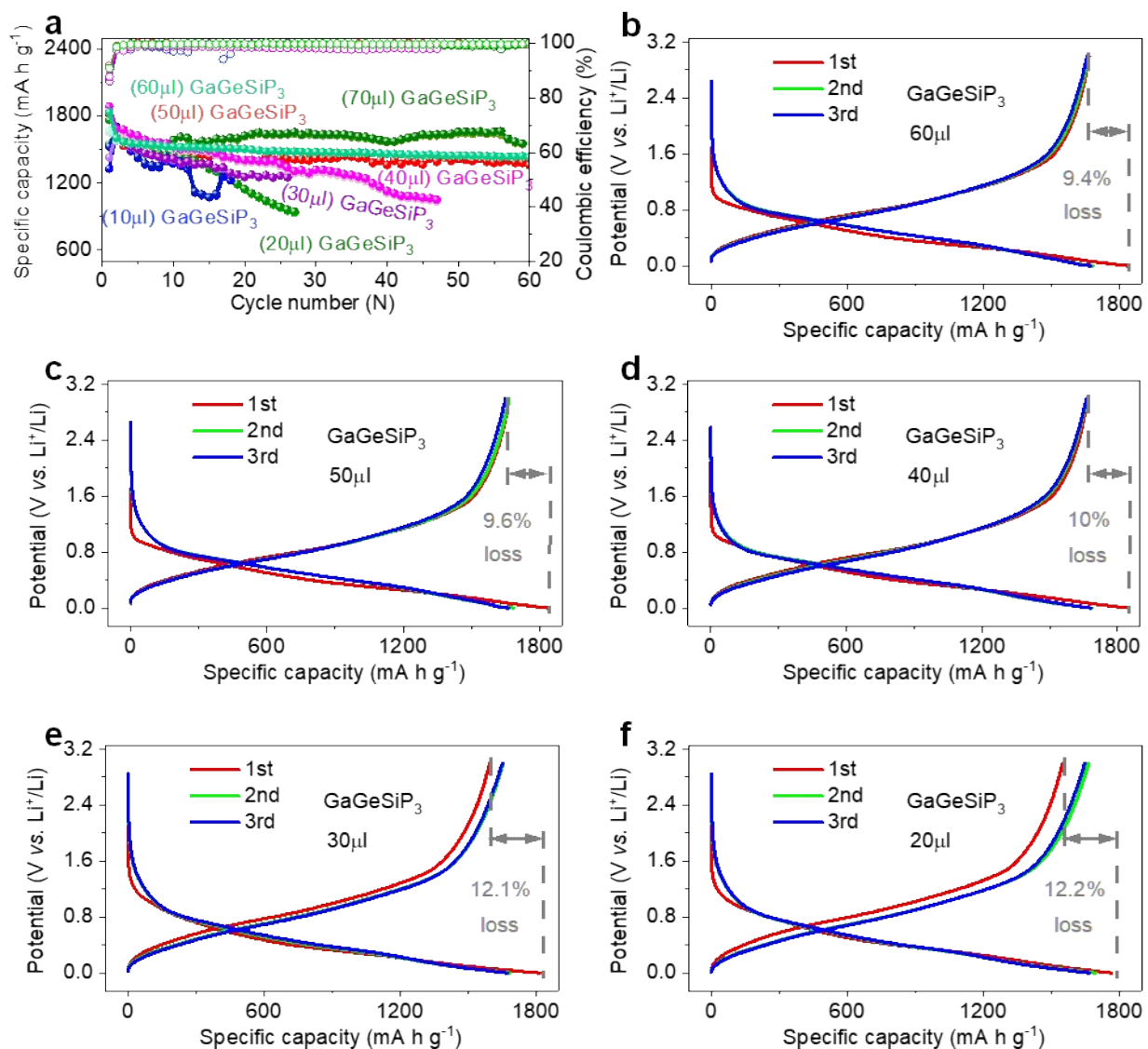

Fig. S20. Cycle performances of GaP+Ge+Si+2P@*x*h samples at 0.4 mA cm^{-2}.
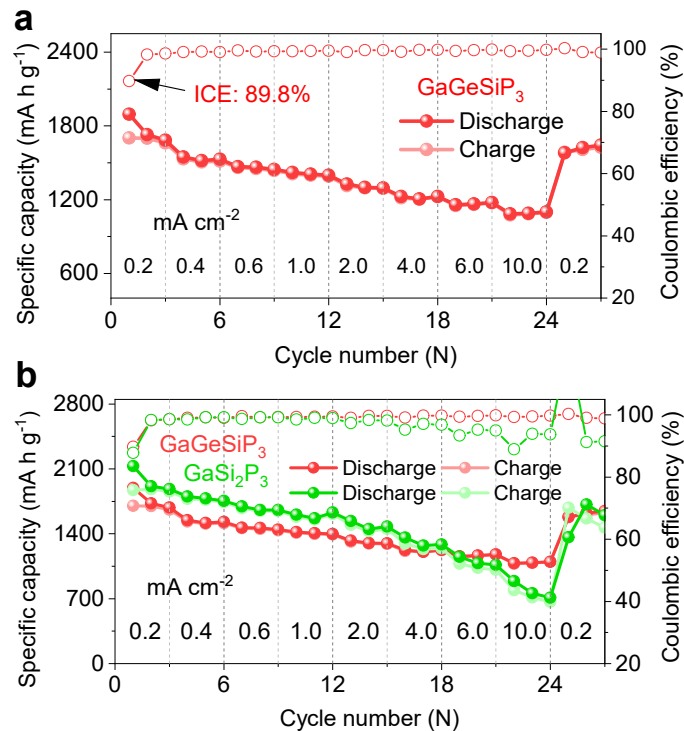
Fig. S21. (a) Rate performance of GaGeSiP$_3$. (b) Rate performances of GaGeSiP$_3$ and GaSi$_2$P$_3$.


Fig. S22. (a) Rate performance of GaGeSiP$_3$. (b) Rate performances of GaGeSiP$_3$ and GaSi$_2$P$_3$.

Fig. S23. (a) The effect of different electrolyte contents on the cycling stability of GaGeSiP$_3$ at 0.4 mA cm^{-2}. (b-f) Initial three GCD profiles of GaGeSiP$_3$ at different electrolyte contents at 0.2 mA cm^{-2}.

The impact of various electrolyte contents on the cycling stability of GaGeSiP$_3$ was investigated, as illustrated in **Fig. S23**. When the electrolyte content falls below 50 μl, the cycling stability deteriorates significantly, attributed to inadequate electrolyte content that fails to facilitate effective Li-ion diffusion. Conversely, surpassing an electrolyte content of 70 μl doesn't yield improved stability, potentially contributing to increased resistance. Notably, maintaining electrolyte levels between 50 and 60 μl leads to enhanced performance (**Fig. S23a**). Additionally, achieving a high Initial Coulombic Efficiency (ICE) ranging from 90.4% to 90.6% is possible (**Fig. S23b-c**). However, GaGeSiP$_3$ exhibits an ICE of only 87.9-87.8% with an electrolyte content below 50 μl (**Fig. S23d-f**), hindering the effective activation of the initial cycle.
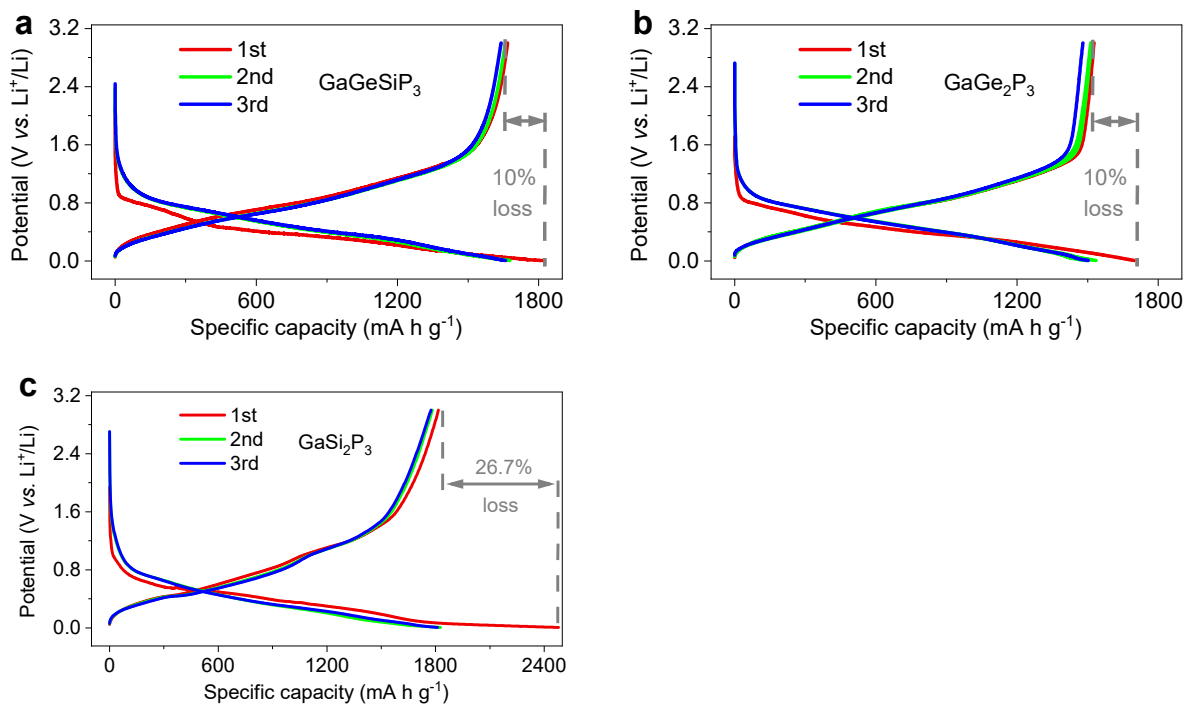
Fig. S24. Initial three GCD profiles with the active materials ratio of 90% at 0.2 mA cm^{-2}. (a) GaGeSiP$_3$. (b) GaGe$_2$P$_3$. (c) GaSi$_2$P$_3$.

We increased the active material ratio to 90%, while maintaining the binder and conductive agents at both 5 wt.%. GaGeSiP$_3$ and GaGe$_2$P$_3$ demonstrate similar Li-storage properties as observed previously. However, the GaSi$_2$P$_3$ electrode displays deteriorated Li-storage properties, including reduced initial Coulombic efficiency, increased polarization, and decreased capacity. This could be attributed to significant volume expansion due to its high silicon content and the presence of inferior electrochemical intermediates.
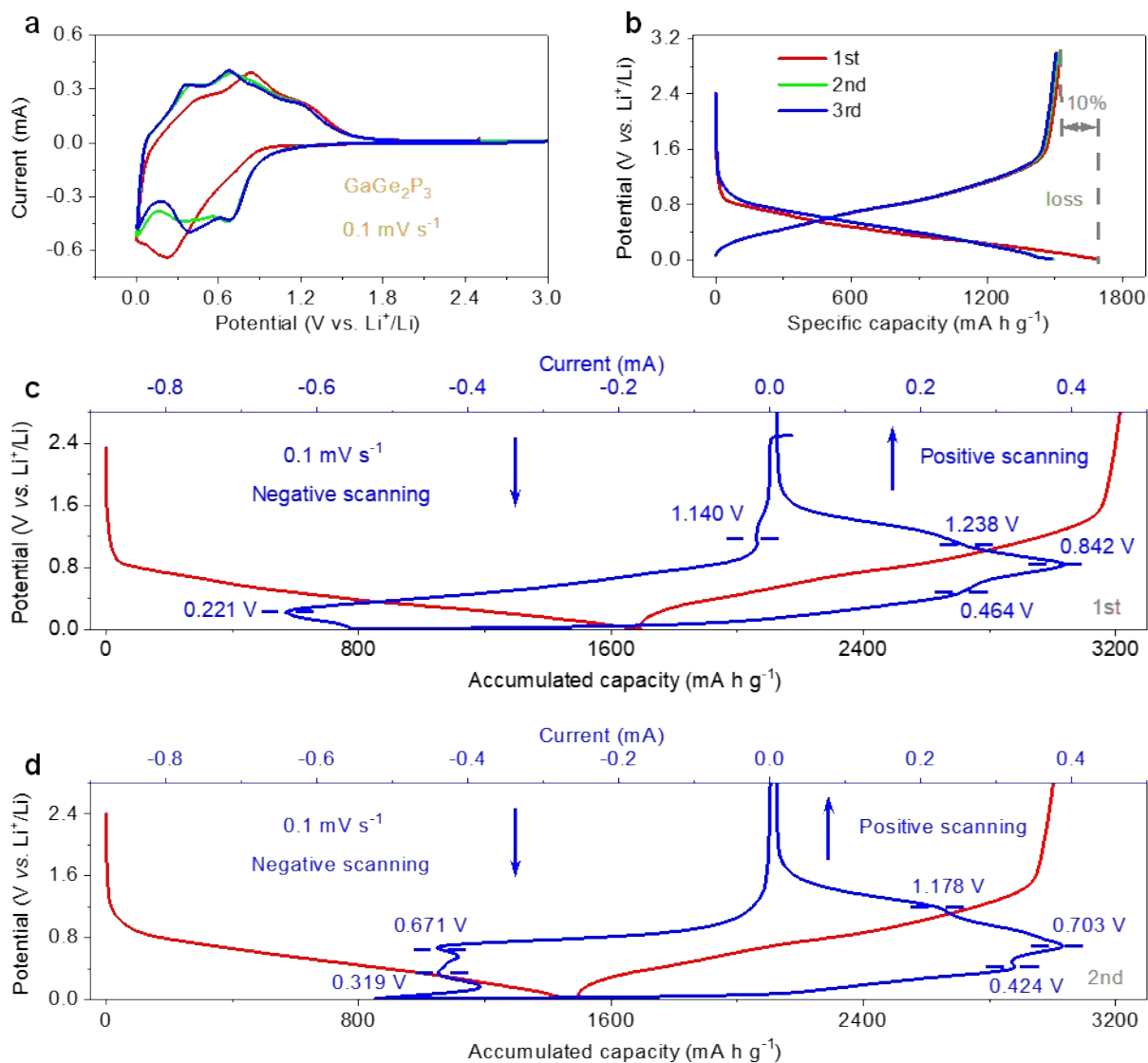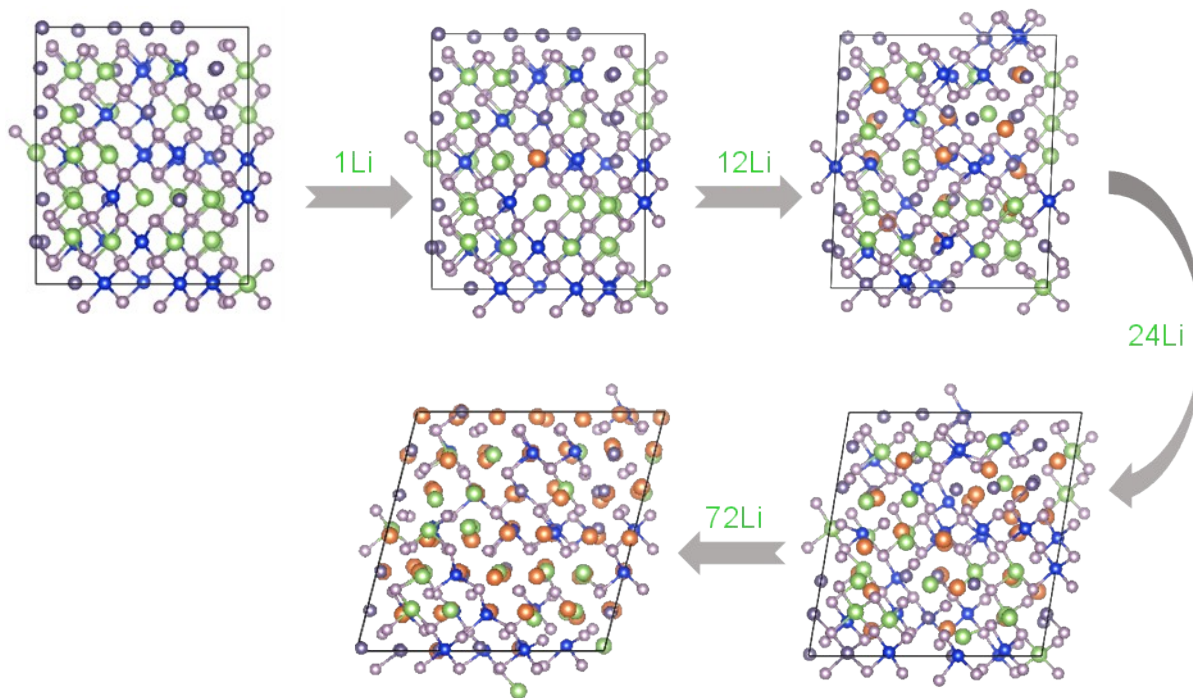
Fig. S25. Electrochemical behaviours of GaGe₂P₃.
(a) Initial three CV profiles at 0.1 mV s⁻¹. (b) Initial three GCD profiles at 0.2 mA cm⁻². (c) First cycle. (d) Second cycle.
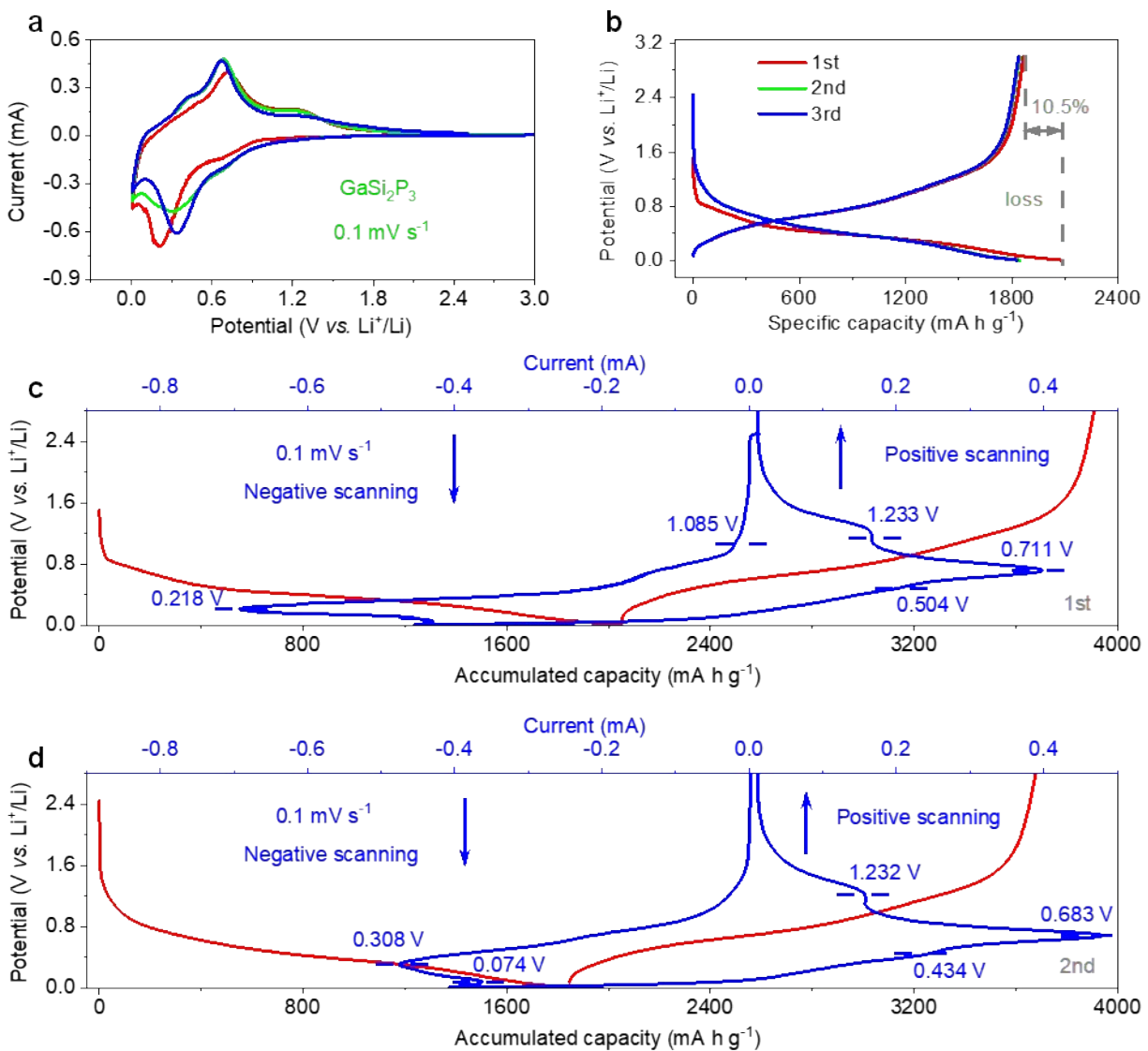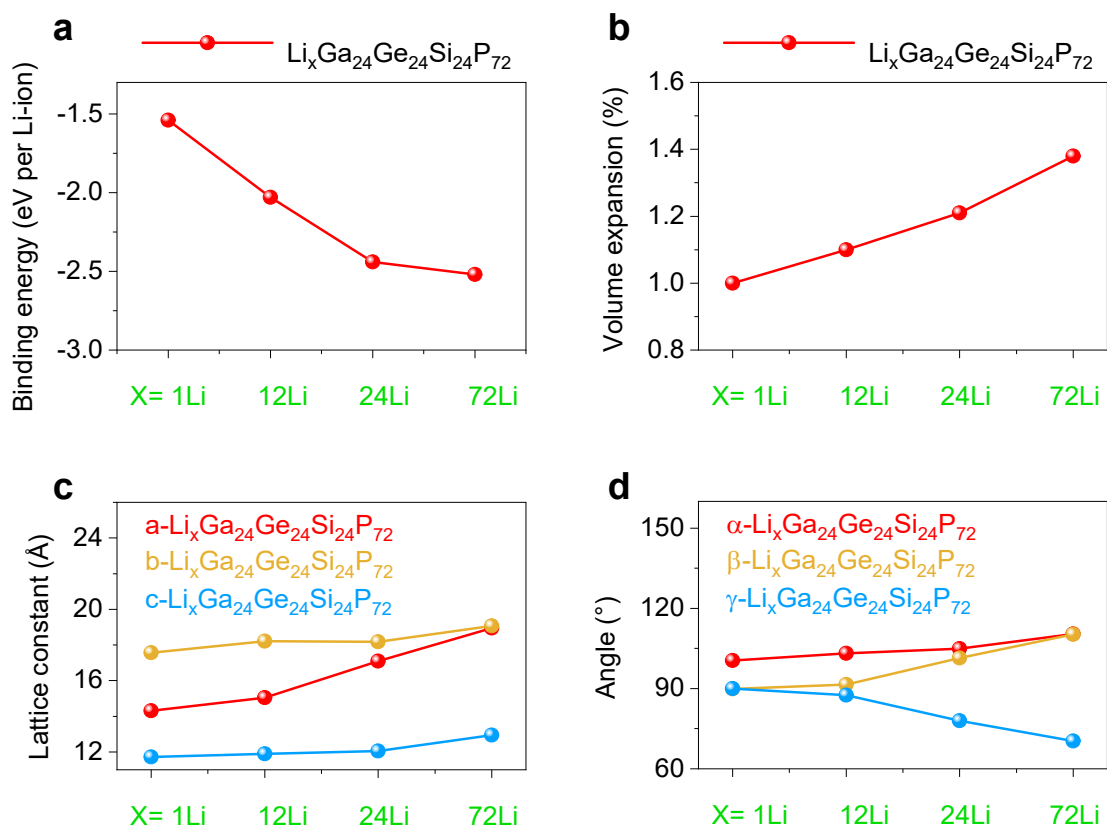
**Fig. S26. Electrochemical behaviours of GaSi$_2$P$_3$**
(a) Initial three CV profiles at 0.1 mV s^{-1}. (b) Initial three GCD profiles at 0.2 mA cm^{-2}. (c) First cycle. (d) Second cycle.

Fig. S27. Supercell models of $Li_xGaGeSiP_3$ (x<3) intermediates.

**Fig. S28.** (a) Binding energies. (b, c, and d) Structural parameters of the $Ga_{24}Ge_{24}Si_{24}P_{72}$-Li, $Ga_{24}Ge_{24}Si_{24}P_{72}$-12Li, $Ga_{24}Ge_{24}Si_{24}P_{72}$-24Li, and $Ga_{24}Ge_{24}Si_{24}P_{72}$-72Li.
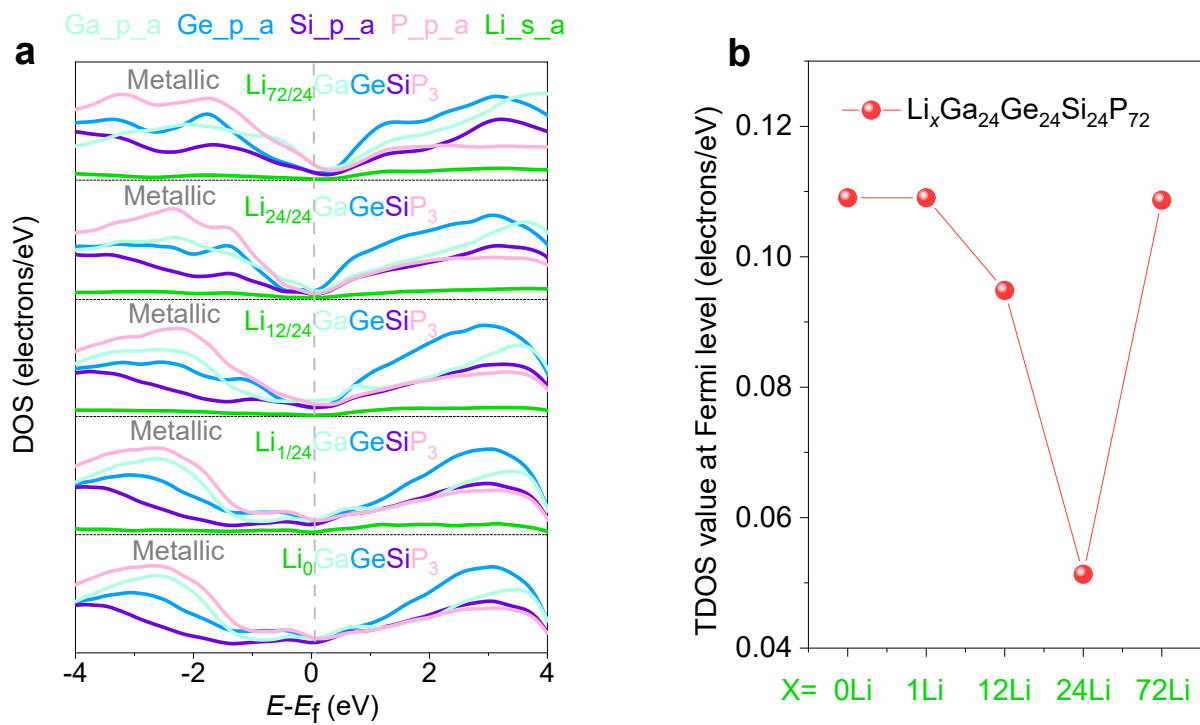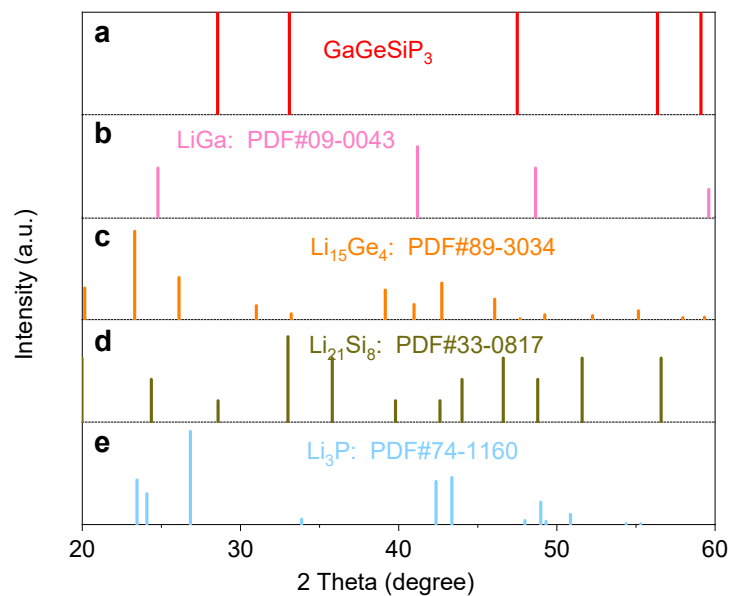
Fig. S29. Metallic conductivity of lithium intercalation compounds.
(a) Partial DOS profiles. (b) Total DOS (TDOS) values at Fermi level of the $Ga_{24}Ge_{24}Si_{24}P_{72}$-Li, $Ga_{24}Ge_{24}Si_{24}P_{72}$-12Li, $Ga_{24}Ge_{24}Si_{24}P_{72}$-24Li, and $Ga_{24}Ge_{24}Si_{24}P_{72}$-72Li as presented in **Fig. S27**.
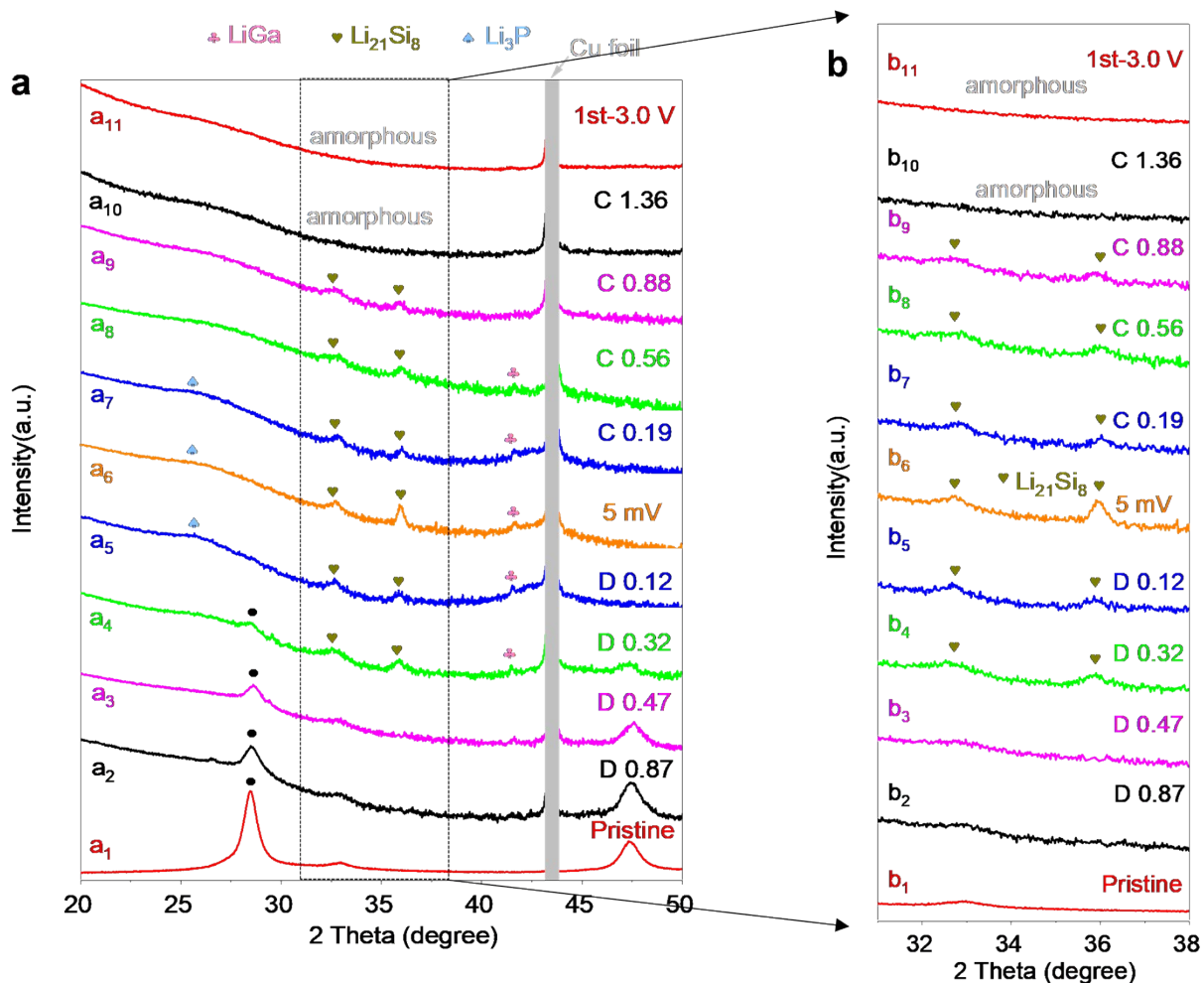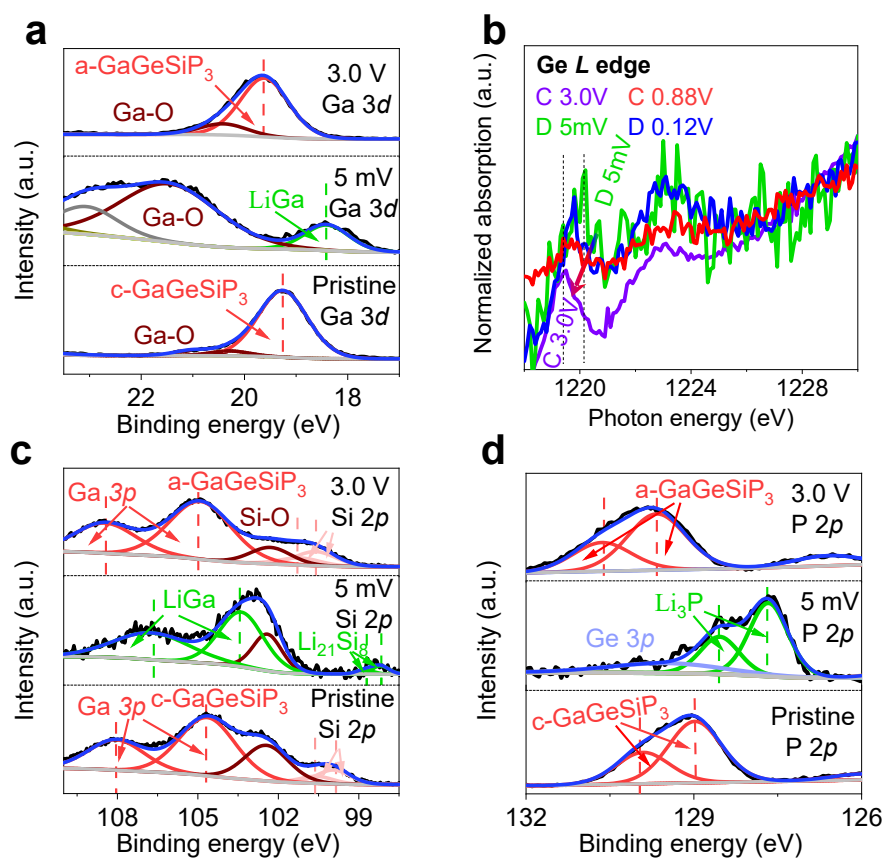
Fig. S30. Ex-situ XRD characterization of GaGeSiP$_3$
(a) 20°-50°. (b) 31°-38°.

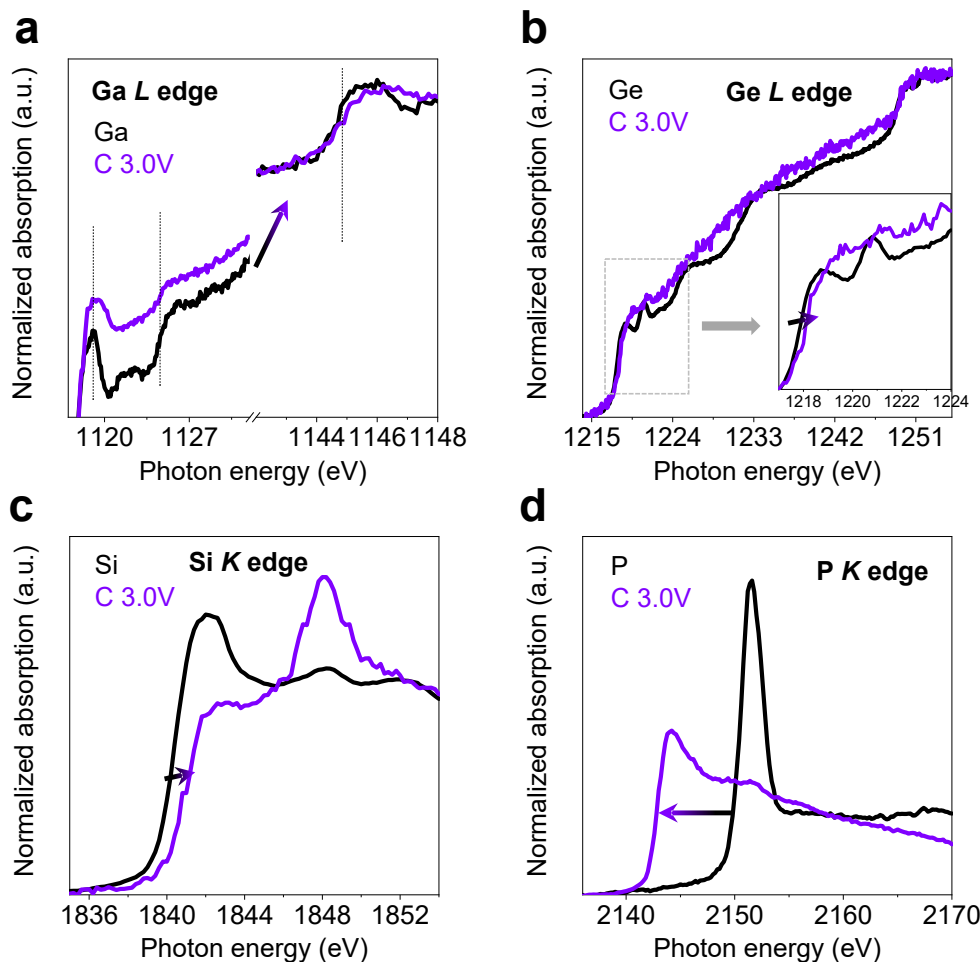**Fig. S31. Standard XRD patterns**

(a) $GaGeSiP_3$. (b) LiGa. (c) $Li_{15}Ge_4$. (d) $Li_{21}Si_8$. (e) Li_3P.

**Fig. S32. Post-mortem spectral characterizations.**

(a, c-d) XPS. (b) XAS spectra of Ge L edge.

Fig. S33. XAS spectra of the GaGeSiP$_3$ electrode charged to 3.0 V and elemental powders. (a) Ga *L* edge. (b) Ge *L* edge. (c) Si *K* edge. (d) P *K* edge.

Compared to the elemental powders of Ga, Ge, and Si, the GaGeSiP$_3$ electrode charged to 3.0 V displayed higher energy levels, suggesting that the elements Ga, Ge, and Si within the GaGeSiP$_3$ electrode charged to 3.0 V carry a positive charge (**Fig. S33a-S33c**). However, phosphorus exhibited an opposite trend, suggesting that the phosphorus derived from the GaGeSiP$_3$ electrode charged to 3.0 V bears a negative charge (**Fig. S33d**).
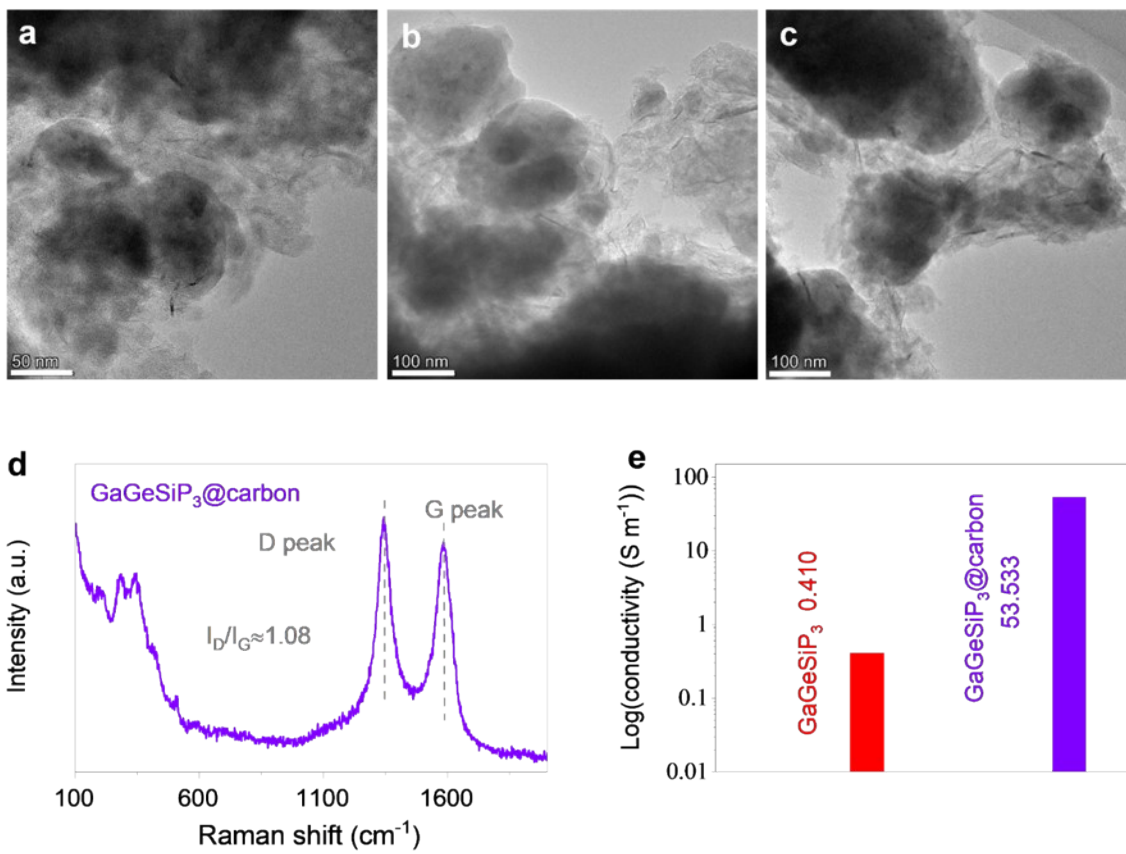
Fig. S34. Structural characteristics of GaGeSiP$_3$@carbon

(a, b, and c) Low-magnification TEM images. (d) Raman spectra. (e) Electronic conductivity.
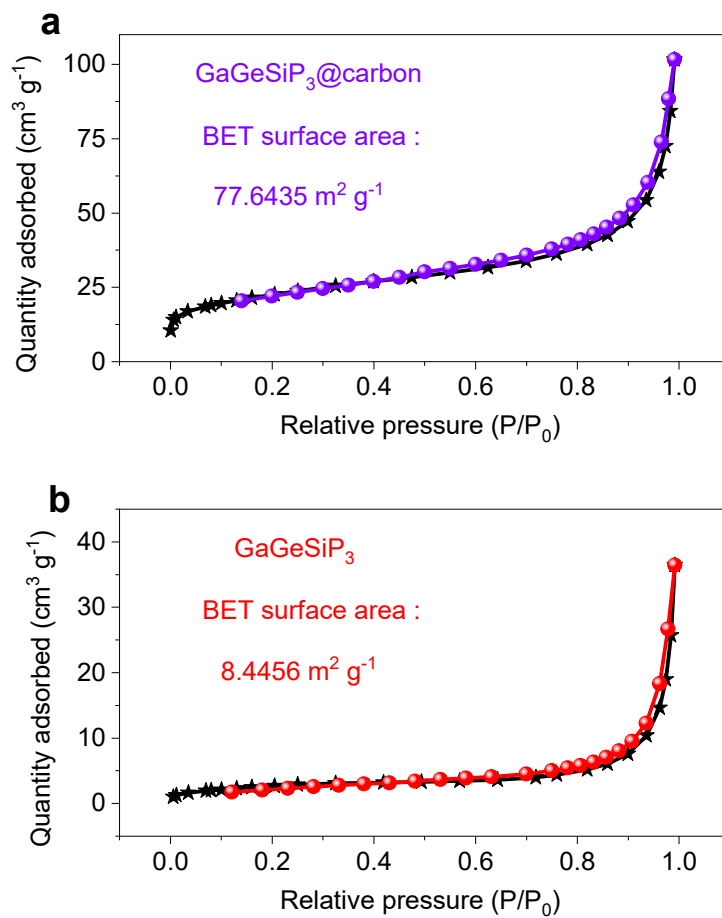
Fig. S35. BET profiles.

(a) GaGeSiP$_3$@carbon. (b) GaGeSiP$_3$.
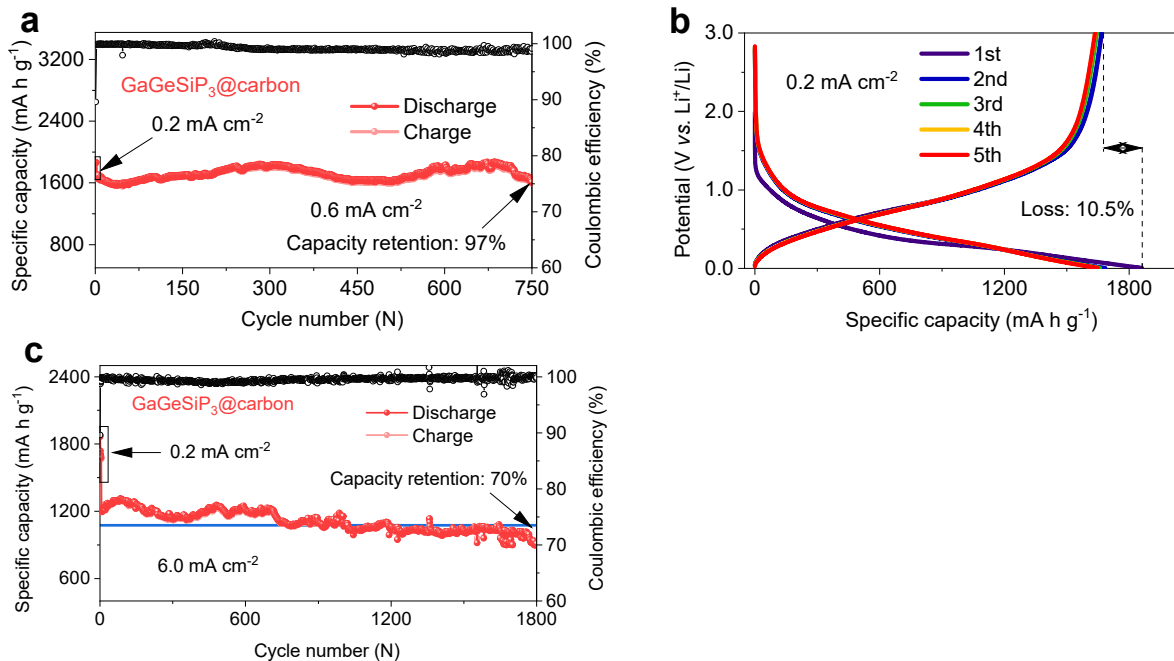
Fig. S36. (a) Cycling stability at 0.6 mA cm^{-2}. (b) Initial five GCD profiles at 0.2 mA cm^{-2}. (c) Long-term cycling stability at 6.0 mA cm^{-2}.
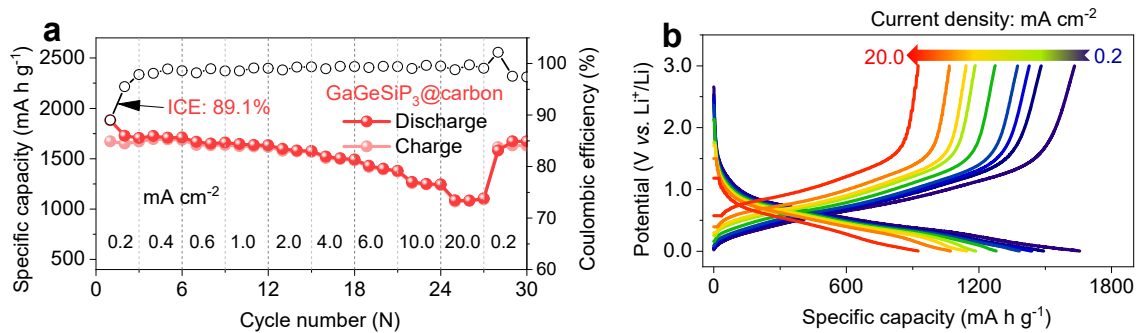
Fig. S37. (a) Rate performance. (b) GCD profiles at different current densities.
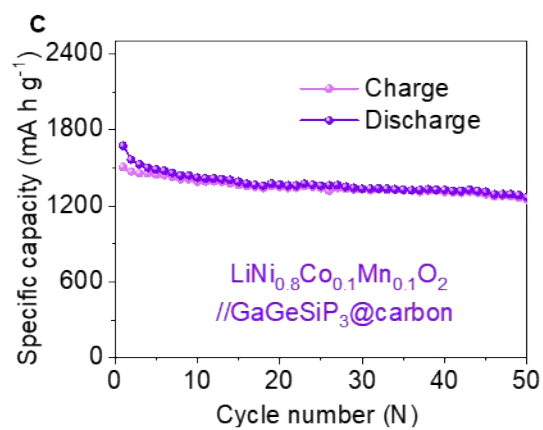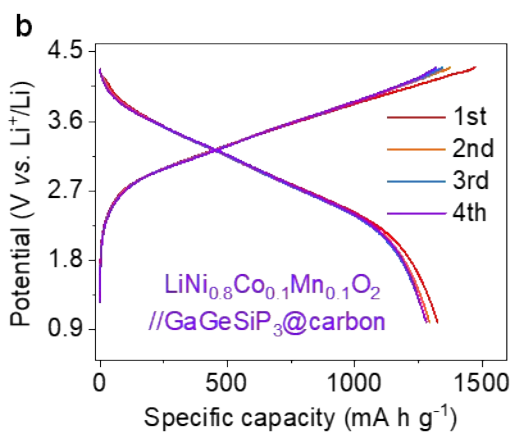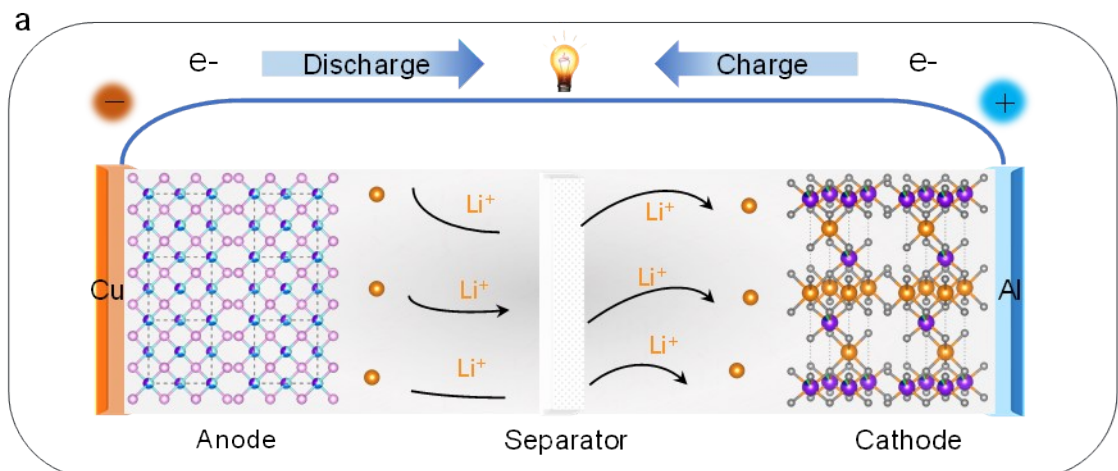
Fig. S38. LiNi$_{0.8}$Co$_{0.1}$Mn$_{0.1}$O$_2$//GaGeSiP$_3$@carbon full cell.

(a) Full cell schematic diagram. (b) First four GCD profiles. (c) Cycle performance at 0.4 mA cm^{-2}.
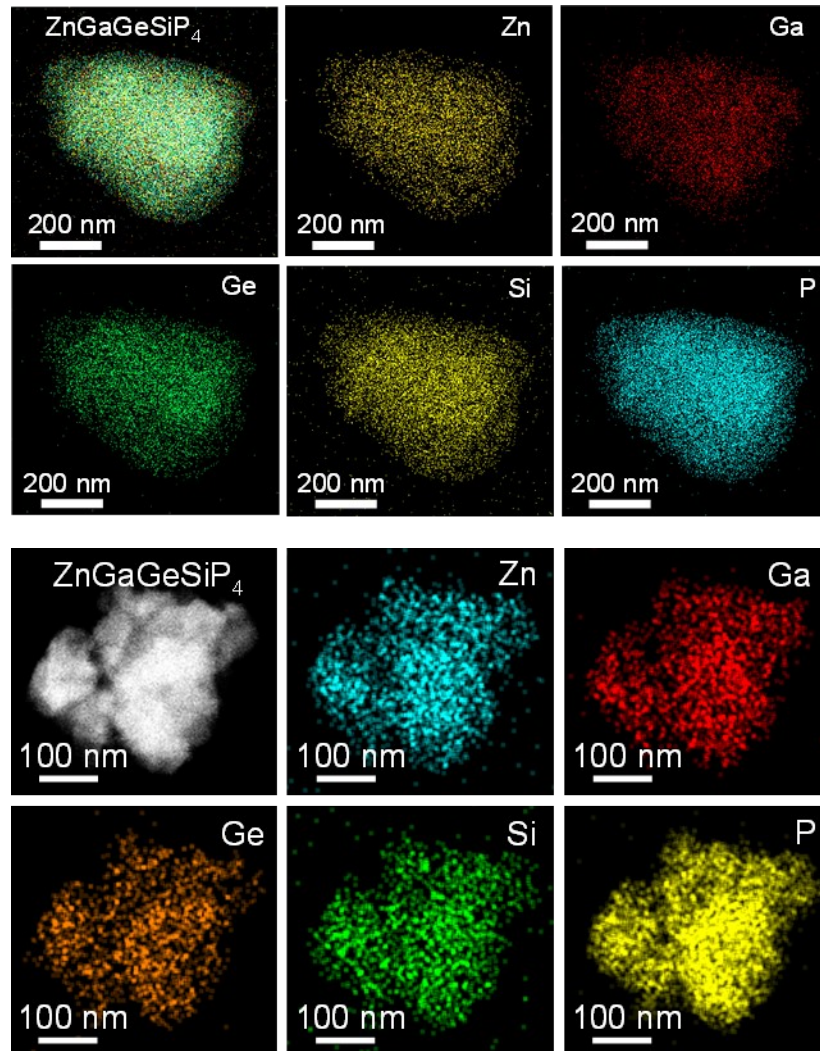
Fig. S39. Elemental mappings of ZnGaGeSiP$_4$.
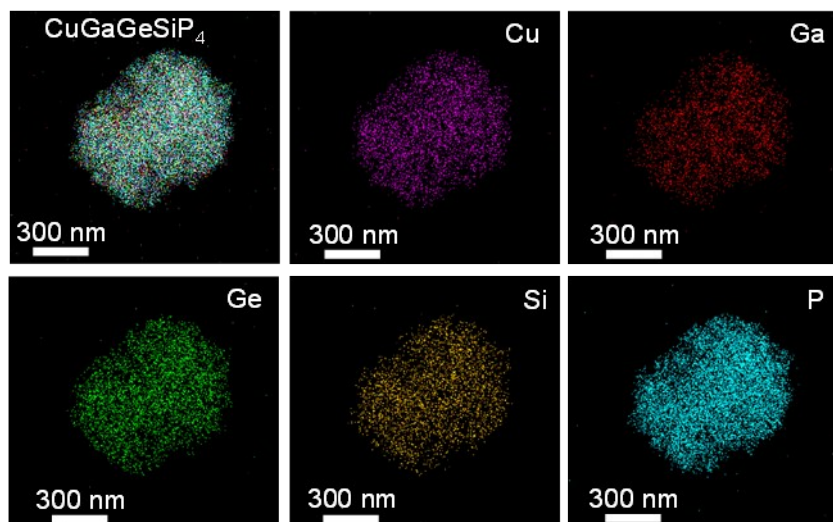
Fig. S40. Elemental mappings of CuGaGeSiP$_4$.
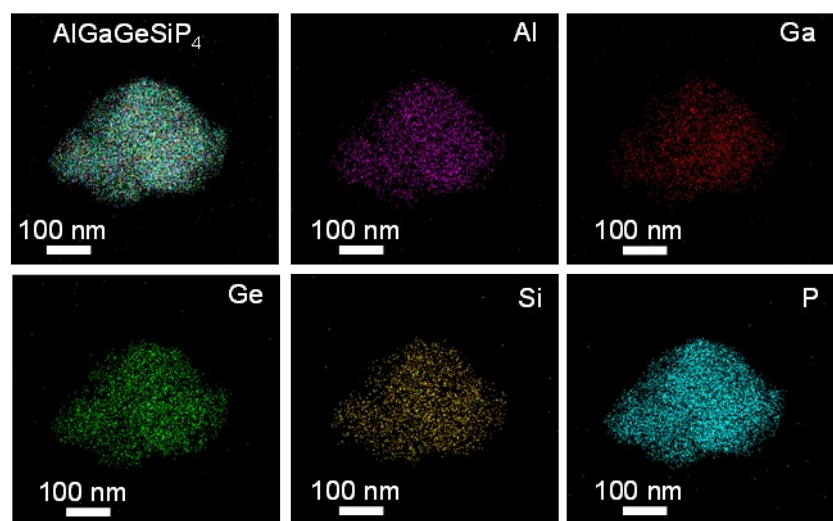
Fig. S41. Elemental mappings of AlGaGeSiP$_4$.
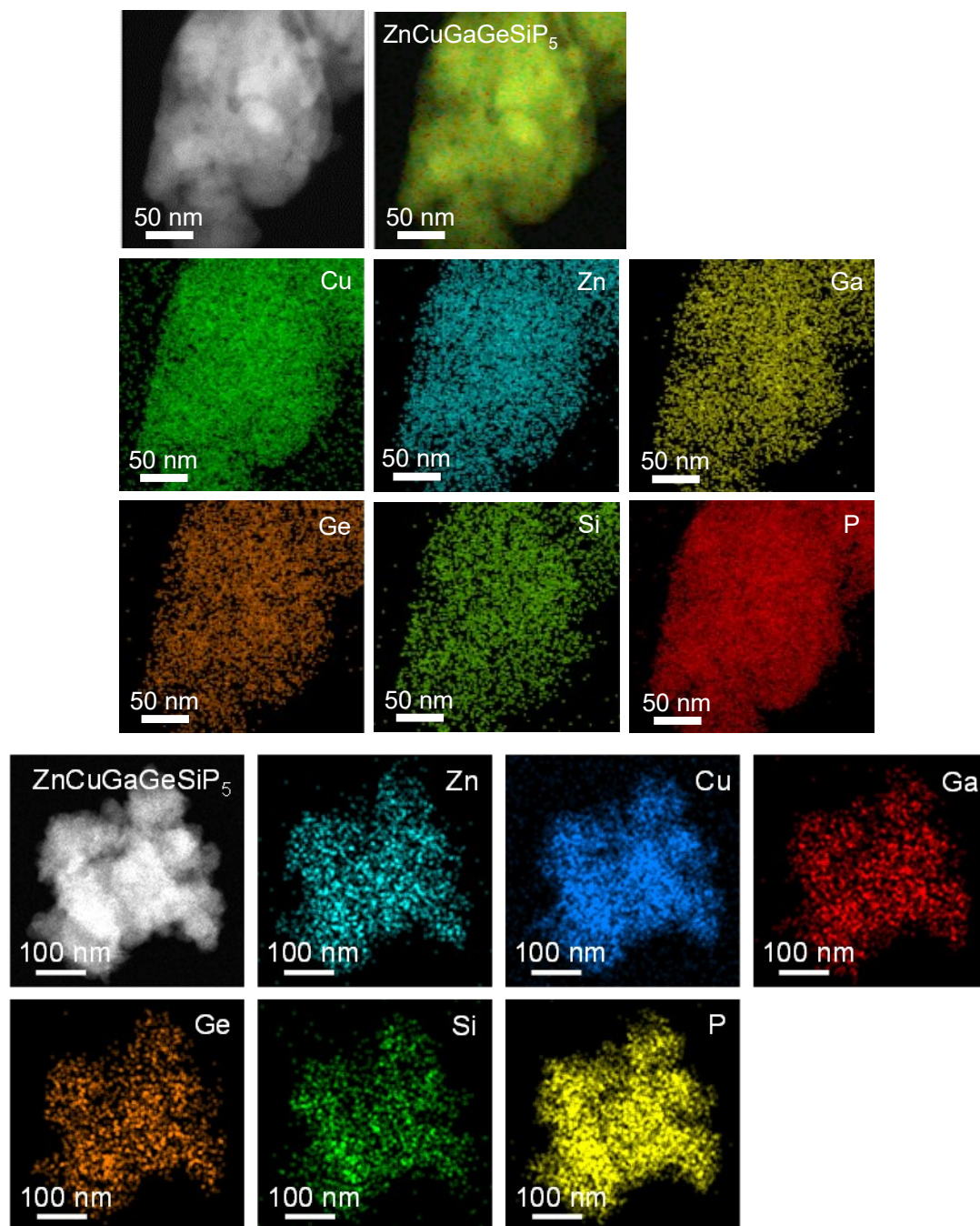
Fig. S42. Elemental mappings of ZnCuGaGeSiP$_5$ at different scales.
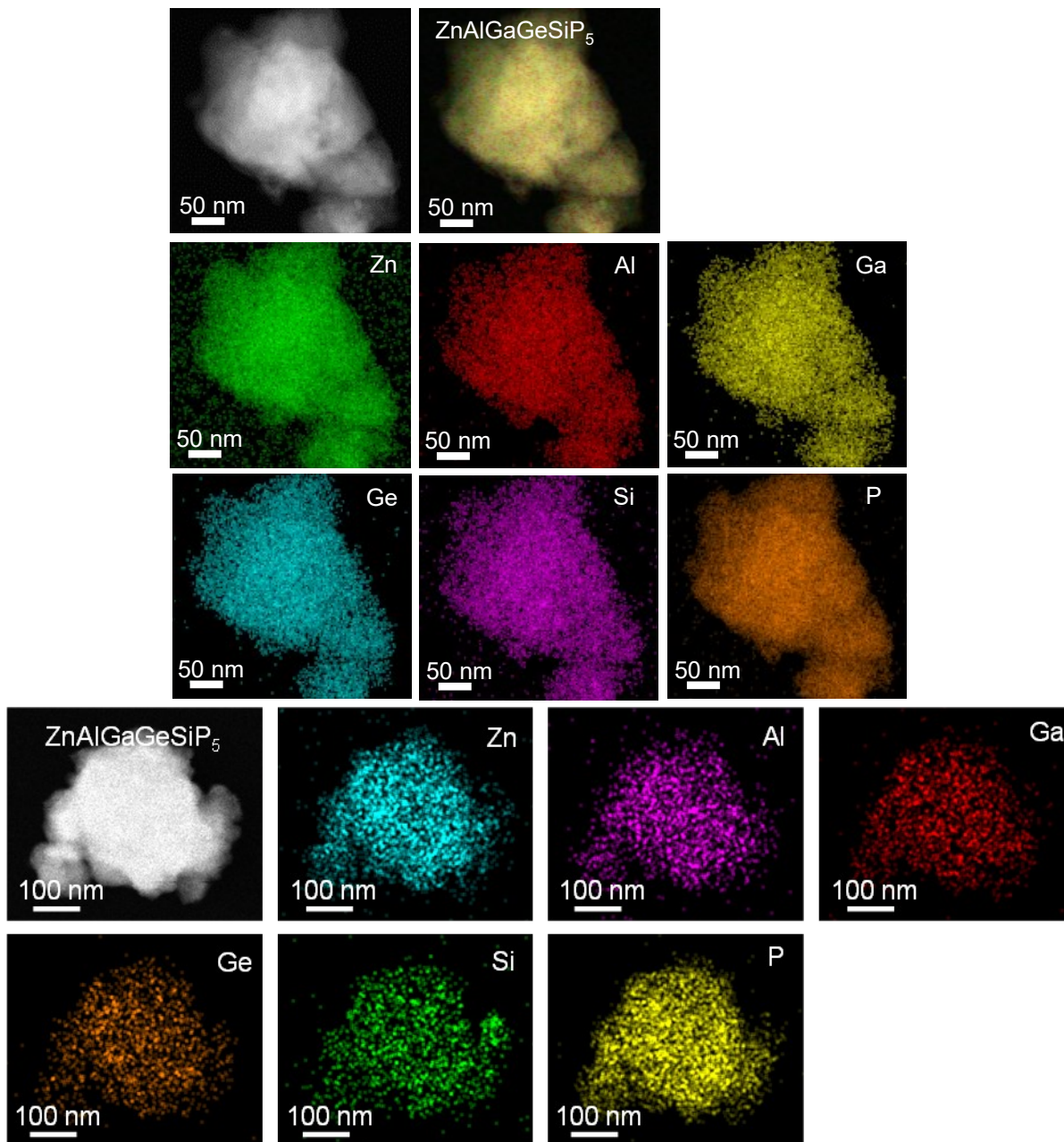
Fig. S43. Elemental mappings of ZnAlGaGeSiP$_5$ at different scales.
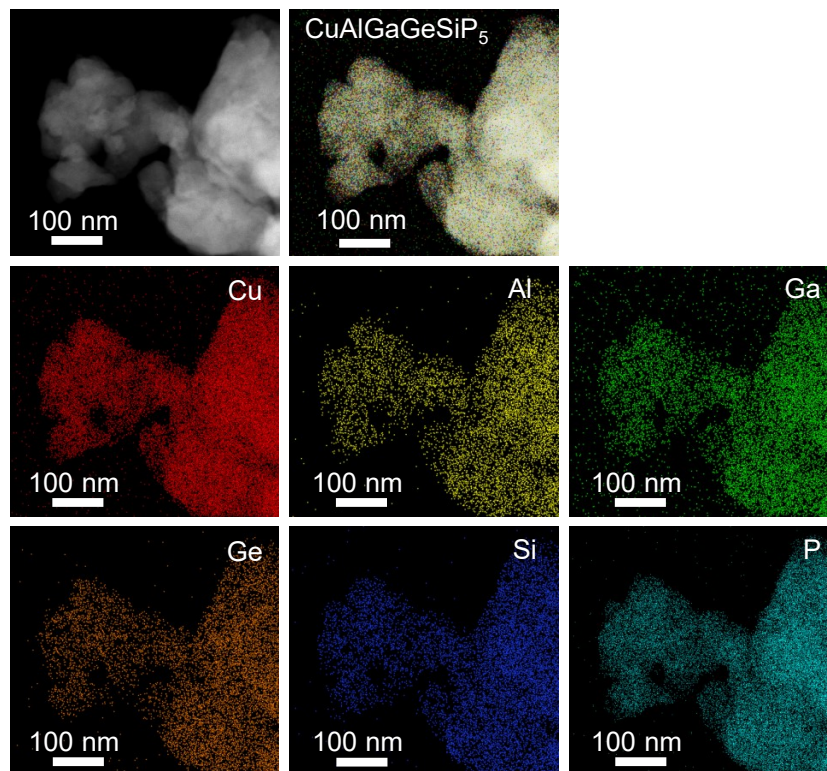
Fig. S44. Elemental mappings of CuAlGaGeSiP$_5$.
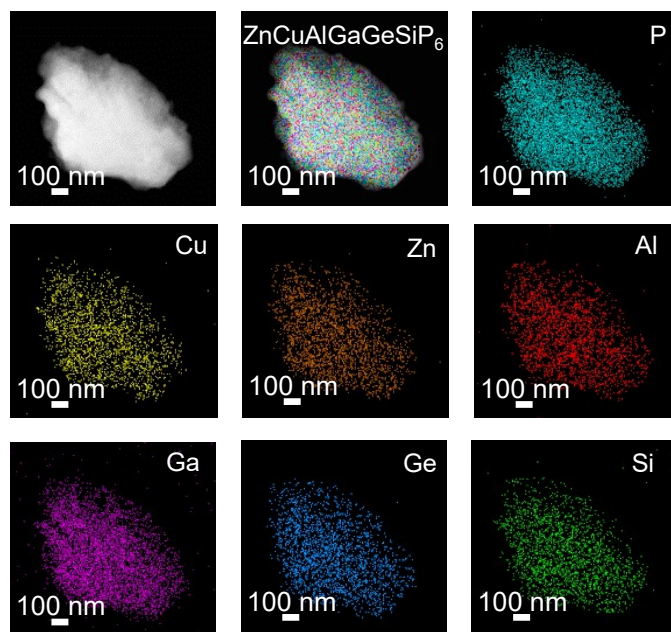
Fig. S45. Elemental mappings of ZnCuAlGaGeSiP$_6$.
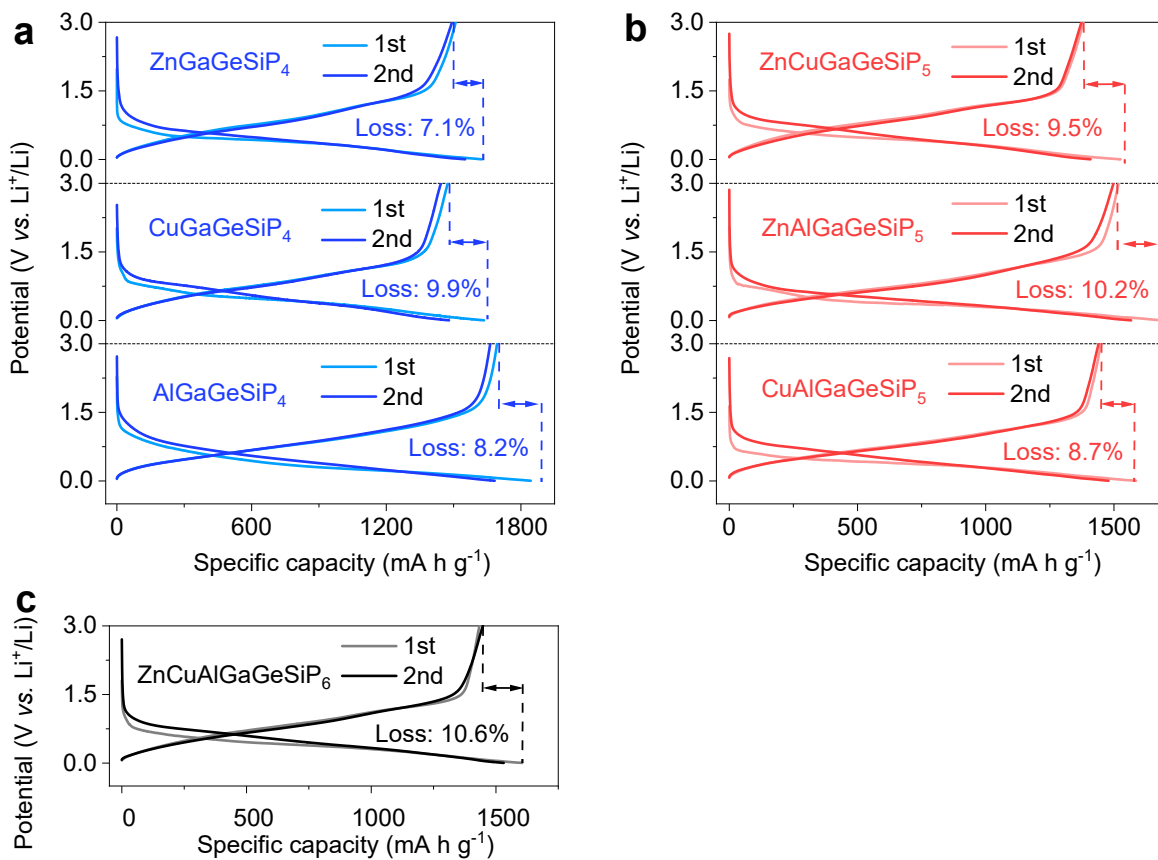
Fig. S46. Initial two GCD profiles at 0.2 mA cm^{-2}.
(a) Quaternary disordered-cation phosphides of ZnGaGeSiP$_4$, CuGaGeSiP$_4$, and AlGaGeSiP$_4$. (b) Pentanary disordered-cation phosphides of ZnCuGaGeSiP$_5$, ZnAlGaGeSiP$_5$, and CuAlGaGeSiP$_5$. (c) Hexanary mixed-cation phosphide of ZnCuAlGaGeSiP$_6$.
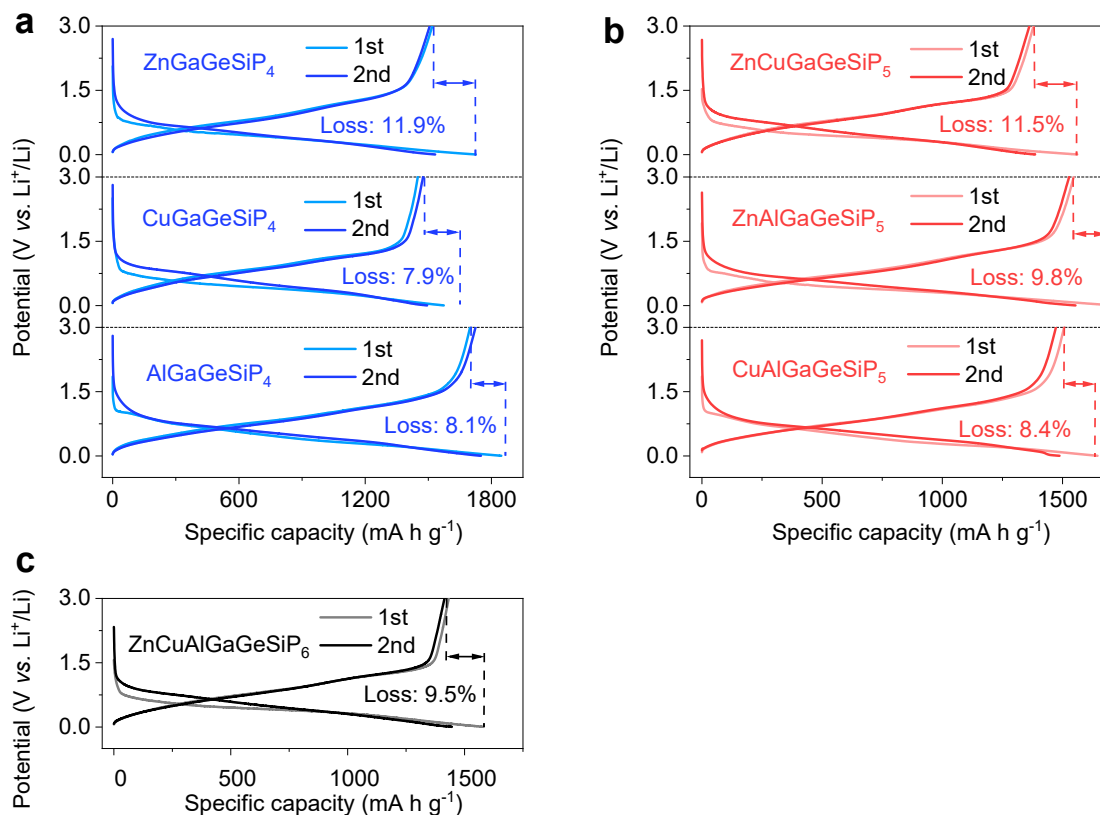
Fig. S47. Initial two GCD profiles with the active materials ratio of up to 90% at 0.2 mA cm^{-2}. (a) Quaternary disordered-cation phosphides of ZnGaGeSiP$_4$, CuGaGeSiP$_4$, and AlGaGeSiP$_4$. (b) Pentanary disordered-cation phosphides of ZnCuGaGeSiP$_5$, ZnAlGaGeSiP$_5$, and CuAlGaGeSiP$_5$. (c) Hexanary mixed-cation phosphide of ZnCuAlGaGeSiP$_6$.
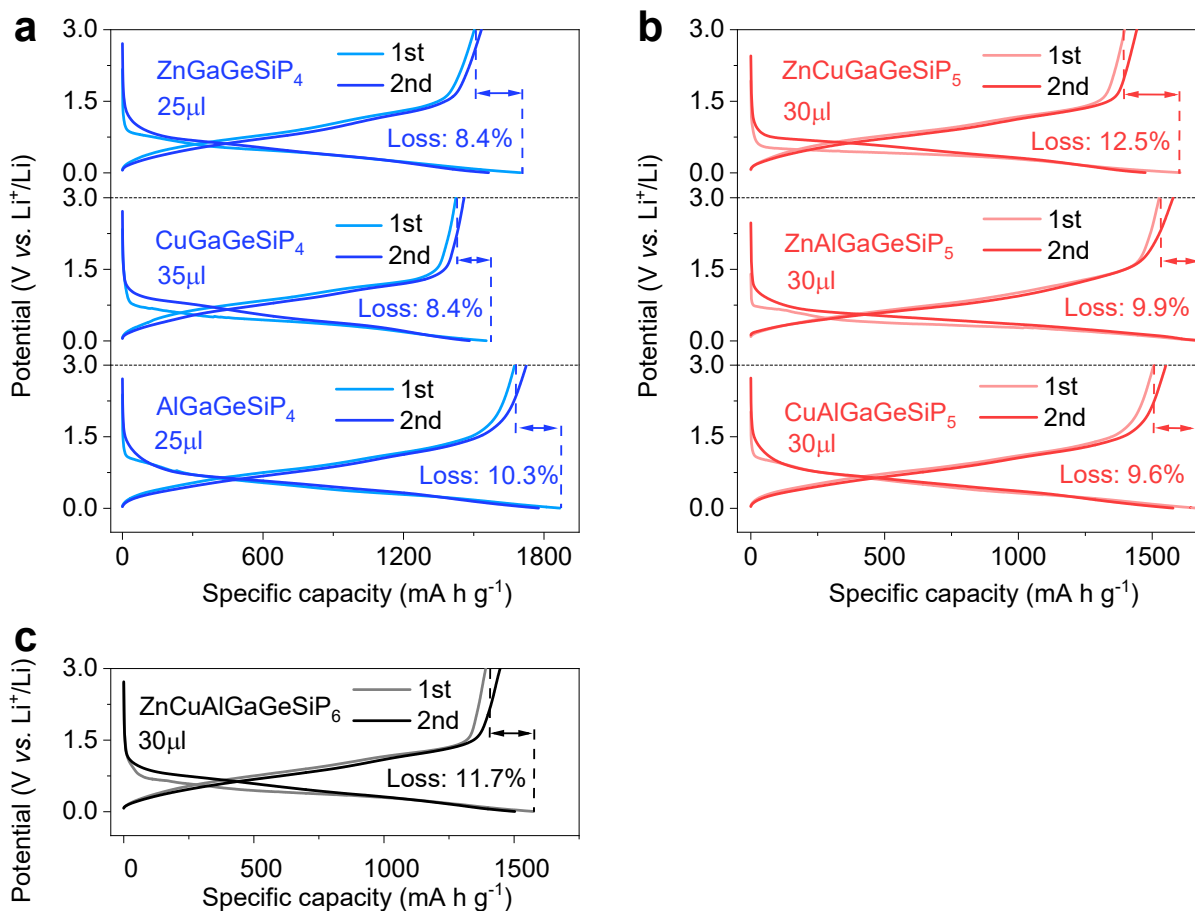
Fig. S48. Initial two GCD profiles with the active materials ratio of up to 90% at different contents of electrolyte at 0.2 mA cm^{-2}.
(a) Quaternary disordered-cation phosphides of ZnGaGeSiP$_4$, CuGaGeSiP$_4$, and AlGaGeSiP$_4$. (b) Pentanary disordered-cation phosphides of ZnCuGaGeSiP$_5$, ZnAlGaGeSiP$_5$, and CuAlGaGeSiP$_5$. (c) Hexanary mixed-cation phosphide of ZnCuAlGaGeSiP$_6$.

As shown in **Fig. S48**, quaternary disordered-cation phosphides of ZnGaGeSiP$_4$, CuGaGeSiP$_4$, and AlGaGeSiP$_4$ and pentanary disordered-cation phosphides (high entropy phosphides) of ZnCuGaGeSiP$_5$, ZnAlGaGeSiP$_5$, and CuAlGaGeSiP$_5$, hexanary mixed-cation phosphides (high entropy phosphide) of ZnCuAlGaGeSiP$_6$ can't achieve high ICE due to low electrolyte contents. Therefore, electrolyte below 50μl can't effectively activate electrode materials. And good performance can be achieved when the electrolyte content is about 50~60 μl **(Fig. S23)**.

Table S1. Fractional atomic coordinates and isotropic displacement parameters of the $GaGeSiP_3$, $GaGe_2P_3$, and $GaSi_2P_3$.

Mater.	Element	x	y	z	B_{iso}	$O_{cc.}$
GaGeSiP$_3$	P	1/4	1/4	1/4	0.02945	1
	Si	0	0	0	0.02500	1/3
	Ge	0	0	0	0.02500	1/3
	Ga	0	0	0	0.00669	1/3
GaGe$_2$P$_3$	P	1/4	1/4	1/4	0.03042	1
	Ge	0	0	0	0.00854	2/3
	Ga	0	0	0	0.47855	1/3
GaSi$_2$P$_3$	P	1/4	1/4	1/4	0.07261	1
	Si	0	0	0	0.00590	2/3
	Ga	0	0	0	0.01570	1/3

Table S2. Main parameters of processing and refinement of the $GaGeSiP_3$, $GaGe_2P_3$, and $GaSi_2P_3$.

Mater. Parameter	GaGeSiP$_3$	GaGe$_2$P$_3$	GaSi$_2$P$_3$
Crystal System	Cubic	Cubic	Cubic
Space Group	F-43m	F-43m	F-43m
V, Å^3	160.103	160.989	157.464
a, Å	5.43	5.44	5.40
2θ-interval°	10-130	10-130	10-130
R_{wp}%	3.15	4.77	5.60
R_p%	2.43	3.64	4.55
χ^2	1.76	1.90	2.56

Table S3. Fractional atomic coordinates and isotropic displacement parameters of the GaGeSiP$_3$ refined from neutron diffraction.

	Element	x	y	z	B$_{iso}$	O$_{cc.}$
GaGeSiP$_3$	P	1/4	1/4	1/4	0.00512(15)	1
	Si	0	0	0	0.00516(49)	1/3
	Ge	0	0	0	0.00696(27)	1/3
	Ga	0	0	0	0.00866(32)	1/3

Table S4. Main parameters of processing and refinement of the GaGeSiP$_3$ refined from neutron diffraction.

Compound	GaGeSiP$_3$
Crystal System	Cubic
Space Group	F-43m
V, Å^3	159.62(1)
a, Å	5.4245(1)
R_{wp}%	1.82
R_p%	1.55
χ^2	0.997

Table S5. Li-ionic diffusion barrier energies of $GaGeSiP_3$, $GaGe_2P_3$, $GaSi_2P_3$, Ge, and Si.

Mater. / Path	$GaGeSiP_3$	$GaGe_2P_3$	$GaSi_2P_3$	Ge	Si
$1 \rightarrow 2$	0.01	0.00	0.05	0.39	0.58
$2 \rightarrow 3$	0.05	0.14	0.59	0.39	0.58
$3 \rightarrow 4$	0.17	0.19	0.06	0.39	0.58
$4 \rightarrow 5$	0.47	0.62	0.71	0.39	0.58
$5 \rightarrow 6$	0.16	0.36	0.39	0.39	0.58
$6 \rightarrow 7$	0.28	0.47	0.40	0.39	0.58
$7 \rightarrow 8$	0.81	0.32	0.42	0.39	0.58
Average	**0.278571**	**0.30**	**0.374286**	**0.39**	**0.58**

Table S6. Elastic constants of $GaGeSiP_3$, $GaGe_2P_3$, $GaSi_2P_3$, Ge, and Si.

Mater. / Direction	$GaGeSiP_3$	$GaGe_2P_3$	$GaSi_2P_3$	Ge	Si
C11	271	609	680	1026	1546
C22	658	1144	1443	1021	1541
C33	474	1203	1513	986	1550
Average	**467.7**	**985.3**	**1212**	**1011**	**1545.7**

3. Supplemental movies:

Movie 1. Raman stretching vibrations of triple disordered-cation GaGeSiP$_3$.
Movie 2. Raman bending and rocking vibrations of triple disordered-cation GaGeSiP$_3$.

References:

1. Z. H. Cui, X. X. Guo and H. Li, *Energy Environ. Sci.*, 2015, **8**, 182-187.
2. A. Nickol, T. Schied, C. Heubner, M. Schneider, A. Michaelis, M. Bobeth and G. Cuniberti, *J. Electrochem. Soc.* , 2020, **167**, 090546.